Stress-displacement stabilized finite element analysis of thin structures using Solid-Shell elements—Part II: Finite strain hyperelasticity

A. Aguirre[a,b], R. Codina[a,c], J. Baiges[a,c], I. Castañar[a]
[a] Universitat Politècnica de Catalunya, Jordi Girona 1 − 3, Edifici C1, Barcelona 08034, Spain.
[b] Universidad de Santiago de Chile, Av. Libertador Bernardo O'Higgins 3363, Estación Central, Santiago, Chile.
[c] Centre Internacional de Mètodes Numèrics en Enginyeria (CIMNE), Gran Capità s/n, Edifici C1, Barcelona 08034, Spain.
alejandro.aguirre@upc.edu (A. Aguirre), ramon.codina@upc.edu (R. Codina), joan.baiges@upc.edu (J. Baiges), icastanar@cimne.upc.edu (I. Castañar)

Abstract

This work is the second of a two-part research project focused on modeling solid-shell elements using a stabilized two-field finite element formulation. The first part introduces a stabilization technique based on the Variational Multiscale framework, which is proven to effectively adress numerical locking in infinitesimal strain problems. The primary objective of the study is to characterize the inherent numerical locking effects of solid-shell elements in order to comprehensively understand their triggers and how stabilized mixed formulations can overcome them. In this current phase of the work, the concept is extended to finite strain solid dynamics involving hyperelastic materials. The aim of introducing this method is to obtain a robust stabilized mixed formulation that enhances the accuracy of the stress field. This improved formulation holds great potential for accurately approximating shell structures undergoing finite deformations. To this end, three techniques based in the Variational Multiscale stabilization framework are presented. These stabilized formulations allow to circumvent the compatibility restriction of interpolating spaces of the unknowns inherent to mixed formulations, thus allowing any combination of them. The accuracy of the stress field is successfully enhanced while maintaining the accuracy of the displacement field. These improvements are also inherited to the solid-shell elements, providing locking-free approximation of thin structures.

Keywords: `Finite strain, Mixed formulations, Solid-Shell elements, Stabilization, Numerical locking`

1. Introduction

Shell structures have become an important research subject in both nature and engineering fields due to their wide-ranging diversity and applicability. However, the structural element technology is a challenging topic due to the inherent unstable behavior when discretized and approximated using numerical methods [1]. In the existing literature, shell models are typically classified into three main categories: classical shell element, continuum-based element, and solid-shell elements. The main distinction among these approaches lies in the treatment of the through-the-thickness integration [2].

The solid-shell approximation of thin structures is well-known to suffer from several types of numerical locking. In Part I of this work [3], extensive investigations were conducted to understand the different mechanisms that trigger numerical locking, which will be briefly discussed here. Among the various types, shear-locking is the most commonly discussed form of numerical locking in the context of shell structures. Shear-locking occurs when the shell fails to accurately couple the in-plane translations of its upper and lower surfaces with the transverse translation of the mid-surface, leading to the emergence of parasitic transverse shear strains [4]. Similarly, membrane-locking arises due to the shell's inability to properly account for the coupling between the in-plane translations of its upper and lower surfaces and the in-plane translation of the mid-surface. This results in the appearance of parasitic membrane strains [5]. Geometrical approximation gives rise to trapezoidal locking, which occurs in solid-shell elements when the director vectors defining the shell's surface are not parallel, leading to the occurrence of parasitic normal transverse strains [6]. Poisson's thickness locking arises due to the incompatibility of the approximation between constant normal transverse strains and linear in-plane strains, which are coupled through Poisson's ratio. Lastly, volumetric locking occurs when the material is nearly or fully incompressible, resulting in the presence of parasitic normal strains [7].

Reduced Integration methods are commonly employed to mitigate certain numerical instabilities by reducing undesired constraints at the quadrature points [8]. However, these approaches are prone to entail spurious zero energy modes [9]. To address this issue, Assumed Strain (AS) methods were developed as a stabilization technique, initially implemented by MacNeal [10] in shell problems. From this point, two of the most utilized stabilization techniques were derived from AS methods: Assumed Natural Strain (ANS) [11] and Enhanced Assumed Strain (EAS) [12] methods. Even though these approaches were initially developed to deal with numerical instabilities in solid mechanic problems, they were eventually extended to classical shell theory and subsequently incorporated into solid-shell elements [13]. Another important approach consists in the Mixed Interpolated Tensorial Components (MITC) method, which has proven to be effective in mitigating numerical locking [14]. In the solid-shell framework, the MITC method has emerged as one of the primary approaches for handling instabilities [15].

The present work deals with the numerical locking by using a mixed two-field approach by introducing additional stresses as new unknowns, thus leading to a problem whose unknowns are stresses and displacements. Note that even though this approach entails a considerable increase in the number of degrees of freedom per node, it also increases the accuracy of the stress and strain fields. In Part I of this work, it has been shown that having control over the stress field allows to correct the parasitic strains arising in thin structures, and also that it is necessary to take as unknowns *all* the components of the stress tensor. However, from the numerical point of view, formulating the problem using a mixed approach leads us to a saddle point problem [16]. This issue stems from the incompatibility between the interpolation spaces of the unknowns, which becomes crucial at this stage. In the context of solid and solid-shell models, utilizing the mixed stress-displacement approach does not permit the use of equal-order interpolation for the variables because it does not fulfill the inf-sup condition. Consequently, careful consideration and treatment are necessary. Hence, the need for stabilization arises. To this end, in this work a stabilized formulation based on the Variational Multiscale (VMS) framework is presented. The VMS approach was first introduced by Hugues [17, 18] and further developed in [19]. This approach was found successful in a wide variety of problems, specially in fluid mechanics [20, 21, 22] and more recently in solid mechanics [23, 24, 25, 26, 27]. By working within the VMS framework, stabilized formulations have been developed, allowing for equal-order interpolation of the unknowns.

This work is organized as follows. The geometrical approximation of the shell domain is briefly explained in Section 2, summarizing the geometrical construction presented in Part I. In Section 3 the solid dynamics equations in finite strain theory are summarized, and a mixed two-field formulation of the problem is stated. The time integration scheme and the linearization method for the non-linear problem are presented in Section 4. The finite element (FE) approximation is presented in Section 5, starting with the Galerkin FE approximation, which requires inf-sup stable interpolations, and then moving to the novel stabilized formulation we propose; as far as we are aware, this is the first work presenting a stabilized displacement-stresss formulation for the finite strain elastic problem. Several numerical examples showing the convergence and accuracy of the proposed method are presented in Section 6. To end up, some conclusions are drawn in Section 7.

2. Geometrical approximation using finite elements

2.1. Construction of the local basis

The details of how the geometry is approximated are explained in Part I of this work; however, for the sake of completeness, they are briefly summarized here. Consider the shell surface to be represented in a general manner by $\Omega^{2\mathrm{D}}$ in $\mathbb{R}^3$. Suppose that we have a FE partition $\mathcal{T}_h = \{K\}$ of $\Omega^{2\mathrm{D}}$ of diameter h, so that $\bar{\Omega}^{2\mathrm{D}} = \bigcup_{K\in\mathcal{T}_h} K$. Let $K \in \mathcal{T}_h$ be an element domain of the partition and its isoparametric mapping

$$\begin{aligned} \boldsymbol{\varphi}_K : K_0 &\longrightarrow K \\ (\xi,\eta) &\mapsto (x^1, x^2, x^3), \end{aligned}$$

that maps the reference domain $K_0 \subset \mathbb{R}^2$ to $K \subset \mathbb{R}^3$, where (ξ,η) are the isoparametric coordinates. Consider a Lagrangian interpolation

$$\boldsymbol{\varphi}_K(\xi,\eta) = \sum_{A=1}^{n_{\mathrm{nod}}} N^A(\xi,\eta)\boldsymbol{x}^A,$$

where n_{nod} is the number of nodes of K, $N^A(\xi,\eta)$ is the shape function of node A on K_0, $A = 1,\dots,n_{\mathrm{nod}}$, and $\boldsymbol{x}^A$ is the position vector of node A in K, $A = 1,\dots,n_{\mathrm{nod}}$. The collection of all mappings $\{\boldsymbol{\varphi}_K, K \in \mathcal{T}_h\}$ provides a local parametrization of $\Omega^{2\mathrm{D}}$.

The vectors tangent to each $K \in \mathcal{T}_h$ are given by

$$\boldsymbol{g}^*_{1,K} = \left|\frac{\partial \boldsymbol{\varphi}_K}{\partial \xi}\right|^{-1} \frac{\partial \boldsymbol{\varphi}_K}{\partial \xi}, \quad \frac{\partial \boldsymbol{\varphi}_K}{\partial \xi} = \sum_{A=1}^{n_{\text{nod}}} \frac{\partial N^A}{\partial \xi} \boldsymbol{x}^A,$$
$$\boldsymbol{g}^*_{2,K} = \left|\frac{\partial \boldsymbol{\varphi}_K}{\partial \eta}\right|^{-1} \frac{\partial \boldsymbol{\varphi}_K}{\partial \eta}, \quad \frac{\partial \boldsymbol{\varphi}_K}{\partial \eta} = \sum_{A=1}^{n_{\text{nod}}} \frac{\partial N^A}{\partial \eta} \boldsymbol{x}^A.$$

These allow us to compute vectors normal to each $K \subset \Omega^{2\text{D}}$ as

$$\boldsymbol{g}^*_{3,K} = \boldsymbol{g}^*_{1,K} \times \boldsymbol{g}^*_{2,K}.$$

If ξ and η are orthogonal coordinates, $|\boldsymbol{g}^*_{3,K}| = 1$; otherwise, $\boldsymbol{g}^*_{3,K}$ is normalized.

The basis vectors $\{\boldsymbol{g}^*_{1,K}, \boldsymbol{g}^*_{2,K}, \boldsymbol{g}^*_{3,K}\}$, are discontinuous across elements if they are only computed in this manner. To obtain a continuous basis we proceed as follows. First, we project the vector field $\boldsymbol{g}^*_{3,K}$, $K \in \mathcal{T}_h$, onto the space of continuous vector fields using a standard $L^2(\Omega^{2\text{D}})$ projection, thus obtaining the nodal vectors $\boldsymbol{g}^a_3$, $a = 1, \ldots, n_{\text{pts}}$, for the nodal points n_{pts} of $\mathcal{T}_h$. Then we have that

$$\boldsymbol{g}_3(x^1, x^2, x^3) = G_3^{-1} \sum_{a=1}^{n_{\text{pts}}} N^a(x^1, x^2, x^3) \boldsymbol{g}^a_3, \quad G_3 = |\sum_{a=1}^{n_{\text{pts}}} N^a(x^1, x^2, x^3) \boldsymbol{g}^a_3|,$$

where N^a is the global shape function of node a. Within each element $K \in \mathcal{T}_h$ we have

$$\boldsymbol{g}_3|_K(\xi, \eta) = G_{3,K}^{-1} \sum_{A=1}^{n_{\text{nod}}} N^A(\xi, \eta) \boldsymbol{g}^A_{3,K}, \quad G_{3,K} = |\sum_{A=1}^{n_{\text{nod}}} N^A(\xi, \eta) \boldsymbol{g}^A_{3,K}|, \tag{2.1}$$

where A is the local numbering of the global node a. Figure 1 shows a cut of a surface and the conceptual difference between $\boldsymbol{g}^*_{3,K}$ and $\boldsymbol{g}_3$. Note that for linear elements $\boldsymbol{g}^*_{3,K}$ will be constant on each $K \in \mathcal{T}_h$.

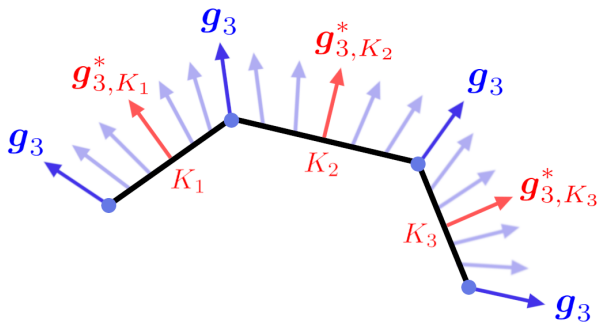

Figure 1: Normal vectors to the shell $\boldsymbol{g}^*_{3,K}$ and their smoothing $\boldsymbol{g}_3$.

Let $\{\boldsymbol{e}_1, \boldsymbol{e}_2, \boldsymbol{e}_3\}$ be the canonical basis of $\mathbb{R}^3$. Once the continuous global vector field $\boldsymbol{g}_3$ is constructed, we can build a continuous local basis at each point $\{\boldsymbol{g}_1, \boldsymbol{g}_2, \boldsymbol{g}_3\}$ by defining

$$\boldsymbol{g}_1 = |\boldsymbol{g}_3 \times \boldsymbol{e}_3|^{-1} \boldsymbol{g}_3 \times \boldsymbol{e}_3, \quad \boldsymbol{g}_2 = \boldsymbol{g}_3 \times \boldsymbol{g}_1, \tag{2.2}$$

the only exception being when $\boldsymbol{g}_3$ aligns with $\boldsymbol{e}_3$, case in which we set $\boldsymbol{g}_1 = \boldsymbol{e}_1$ and $\boldsymbol{g}_2 = \boldsymbol{e}_2$ or $\boldsymbol{g}_1 = -\boldsymbol{e}_1$ and $\boldsymbol{g}_2 = -\boldsymbol{e}_2$ if $\boldsymbol{g}_3$ is opposite to $\boldsymbol{e}_3$. The covariant basis $\{\boldsymbol{g}_1, \boldsymbol{g}_2, \boldsymbol{g}_3\}$ constructed this way will be such that $\{\boldsymbol{g}_1, \boldsymbol{g}_2\}$ will be *approximately* tangent to $\Omega^{2\text{D}}$ and $\boldsymbol{g}_3$ *approximately* normal. The curvilinear coordinates $(\theta^1, \theta^2, \theta^3)$ are then defined as those tangent to $\{\boldsymbol{g}_1, \boldsymbol{g}_2, \boldsymbol{g}_3\}$ at each point.

2.2. Extrusion of the shell mid-surface

The domain $\Omega^{2\text{D}}$ represents the mid-surface of the shell. The solid-shell domain where the calculations are performed is denoted as $\Omega^{3\text{D}}$, and it is computed from the extrusion of $\Omega^{2\text{D}}$ in the normal direction. The construction of $\Omega^{3\text{D}}$ can be done element-wise due to the continuity of $\boldsymbol{g}_3$.

Consider the thickness of the shell to be defined by its values at the nodes of $\mathcal{T}_h$, denoted as t^a, $a = 1, \dots n_{\text{pts}}$. For each $K \in \mathcal{T}_h$, the thicknesses at the nodes will be t_K^A, A being the local number of node a, and we can construct the thickness function

$$t_K(\xi, \eta) = \sum_{A=1}^{n_{\text{nod}}} N^A(\xi, \eta) t_K^A.$$

From the reference element K_0 we can construct the 3D reference element $K_0^{\text{3D}} = K_0 \times [-1, 1]$ and the mapping

$$\begin{aligned} &\boldsymbol{\psi}_K : K_0^{\text{3D}} \longrightarrow \mathbb{R}^3 \\ &\quad (\xi, \eta, \zeta) \mapsto (x^1, x^2, x^3) = \boldsymbol{\varphi}_K(\xi, \eta) + \zeta \frac{1}{2} t_K(\xi, \eta) \boldsymbol{g}_3|_K(\xi, \eta), \end{aligned} \tag{2.3}$$

and then set $K^{\text{3D}} = \boldsymbol{\psi}_K(K_0^{\text{3D}})$, i.e., the image of K_0^{3D} through $\boldsymbol{\psi}_K$. The solid domain where the problem is posed is then $\Omega^{\text{3D}} = \bigcup_{K \in \mathcal{T}_h} K^{\text{3D}}$. From the continuity of $\boldsymbol{g}_3$ and the intrinsic continuity of the thickness function, Ω^{3D} will be a smooth extrusion of Ω^{2D}. This domain, together with the systems of coordinates and basis introduced so far, are depicted in Fig. 2. Since we are interested in solids of small thickness, we shall take the basis $\{\boldsymbol{g}_1, \boldsymbol{g}_2, \boldsymbol{g}_3\}$ as constant across the thickness of the shell.

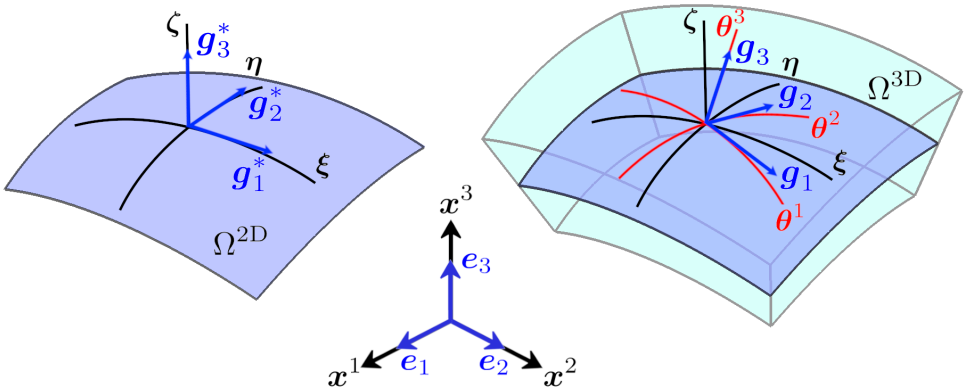

Figure 2: Geometry of the shell: 2D surface (left) and 3D extruded volume (right).

2.3. Interpolation across the thickness

Once the element domains $\{K^{\text{3D}}\}$ have been constructed, we need to define their degrees of freedom and a basis for the FE space we wish to construct. As for the original partition $\{K\}$, we shall consider continuous Lagrangian interpolations, and it suffices to define them for the reference element $K_0 \times [-1, 1]$. Let $N_i^{A,A'}(\xi, \eta, \zeta)$ be the shape function of a node in $K_0 \times [-1, 1]$ that corresponds to node A of K_0 and node A' of the discretization of $[-1, 1]$. The shape functions corresponding to the shell body $N_i^{A,A'}(\xi, \eta, \zeta)$ can now be constructed by multiplying the mid-surface shape functions $N^A(\xi, \eta)$ and the standard one dimensional Lagrangian shape functions $N^{A'}(\zeta)$ in the isoparametric space:

$$N^{A,A'}(\xi, \eta, \zeta) = N^A(\xi, \eta) N^{A'}(\zeta). \tag{2.4}$$

At the global level the shape functions will be written as $N^a(x^1, x^2, x^3)$, with a running again from 1 to n_{pts}. The FE partition resulting from the extrusion of the FE partition of the shell surface $\mathcal{T}_h = \{K\}$ will be denoted as $\mathcal{T}_h^{\text{3D}} = \{K^{\text{3D}}\}$. From this point forward, the superscript 3D will be omitted for simplicity, since the following formulations as well as the numerical experiments are presented by considering the 3D approximation of the shell.

3. Continuous solid dynamics problem

In the Part I of this work, a comprehensive analysis of locking mechanisms in thin structures was conducted. This was achieved by formulating the linear elastic problem in curvilinear coordinates using a mixed stress-displacement approach. It was observed that interpolating specific components of the stress tensor allowed to overcome certain types of numerical locking. However, it was concluded that the most robust formulation is achieved by interpolating

the entire stress tensor, as this approach is capable of addressing all types of locking in any given problem. Since the interpolation of the complete stress tensor is necessary, there is no advantage in using curvilinear coordinates. Therefore, the following problem is formulated in Cartesian coordinates. This work presents the finite strain solid dynamics problem using a total Lagrangian description in relation to a Cartesian basis. The equations are written employing index notation; therefore, repeated indexes imply summation over the spatial dimensions. Furthermore, lowercase and uppercase indices denote variables evaluated in the current and material configurations, respectively.

3.1. Conservation equations

Consider a solid shell occupying a domain $\Omega(t)$ of $\mathbb{R}^d$ at the current time $t \geqslant 0$, where $d \in \{2, 3\}$ is the number of space dimensions; $\Omega(t)$ is thus the current configuration at time t. Let $\Gamma(t) = \partial\Omega(t)$ be its boundary, whereas the counterparts of $\Omega(t)$ and $\Gamma(t)$ in the reference configuration are denoted by $\Omega_0 = \Omega(0)$ and $\Gamma_0 = \partial\Omega_0$, respectively. Let us consider the motion $\boldsymbol{\phi}$ of the deformable body through a time interval $]0, T[$, described by the mapping $\boldsymbol{\phi} : \Omega_0 \to \Omega(t)$ between the initial and current configurations, whose particles are labeled in the coordinates $\boldsymbol{X} \in \Omega_0$ and $\boldsymbol{x} \in \Omega(t)$, respectively, as follows

$$\boldsymbol{x} = \boldsymbol{\phi}\left(\boldsymbol{X}, t\right). \tag{3.1}$$

The linear momentum conservation equation in finite strain theory, in the total Lagrangian framework, reads

$$\rho_0 \frac{\partial^2 u_a}{\partial t^2} - \frac{\partial}{\partial X_A}\{F_{aB} S_{BA}\} = \rho_0 b_a \quad \text{in } \Omega_0 \times]0, T[\,, \tag{3.2}$$

where ρ_0 is the initial density, $\boldsymbol{F} = \frac{\partial \boldsymbol{x}}{\partial \boldsymbol{X}}$ is the deformation gradient, $\boldsymbol{S}$ is the second Piola-Kirchhoff (PK2) stress tensor and $\rho_0 \boldsymbol{b}$ are the body forces. Note that the angular momentum equation implies the symmetry of the PK2 stress tensor. The mass conservation equation can be written as

$$\rho J = \rho_0, \tag{3.3}$$

where ρ is the density at the current time t and $J = \det(\boldsymbol{F}) > 0$ is the determinant of the deformation gradient.

3.2. Constitutive model

Let us consider non-linear isotropic hyperelastic models, based in a strain energy function Ψ that measures the work done by stresses from the initial to the current configuration. The PK2 stress tensor can be written in terms of the strain energy function by taking derivatives with respect to the right Cauchy-Green tensor $\boldsymbol{C} = \boldsymbol{F}^T \cdot \boldsymbol{F}$ as

$$\boldsymbol{S} = 2\frac{\partial \Psi(\boldsymbol{C})}{\partial \boldsymbol{C}}. \tag{3.4}$$

This work only deals with isotropic materials; therefore the relationship between Ψ and $\boldsymbol{C}$ must be independent of the coordinate system chosen. For this reason, Ψ is built as a function of the invariants of $\boldsymbol{C}$, defined as

$$\begin{aligned} I_1 &= \operatorname{trace}(\boldsymbol{C}) = \boldsymbol{C} : \boldsymbol{I}, \\ I_2 &= \operatorname{trace}(\boldsymbol{C} \cdot \boldsymbol{C}) = \boldsymbol{C} : \boldsymbol{C}, \\ I_3 &= \det(\boldsymbol{C}) = J^2. \end{aligned}$$

The compressible Neo-Hookean material stored energy function can now be defined in terms of the invariants as

$$\Psi = \frac{\mu}{2}\left(I_1 - 3\right) - \mu \ln J + \frac{\lambda}{2}\left(\ln J\right)^2 \tag{3.5}$$

where μ and λ are material coefficients. Note that in a rigid body motion, or absence of deformation, the deformation gradient is zero and the stored energy function vanishes. Note also that the present approach does not contemplate solving incompressible materials, as presented in [23, 24]. However, it is possible to adopt a decoupled representation of the strain energy function into the deviatoric and volumetric parts, allowing the use of different models for each component. In the particular case of compressible Neo-Hookean materials, the expression for the PK2 stress tensor can be obtained from Eq. (3.4) as

$$\boldsymbol{S} = \mu\left(\boldsymbol{I} - \boldsymbol{C}^{-1}\right) + \lambda\left(\ln J\right)\boldsymbol{C}^{-1}. \tag{3.6}$$

3.3. Governing equations

The solid mechanics problem is presented through a two-field formulation, using both the PK2 stresses and the displacements as unknowns; a novel FE approximation will be proposed for the resulting problem. The interpolation of $\boldsymbol{S}$ allows to obtain a higher accuracy in the computation of stresses in finite strain problems and, in the case of shells, it also allows to overcome numerical locking when dealing with thin structures, as it has been shown in the infinitesimal strain case [28]. For this purpose, let us construct the mathematical framework for the present formulation. Consider the space-time domain $\boldsymbol{\mathcal{D}} = \{(\boldsymbol{X}, t) \,|\, \boldsymbol{X} \in \Omega_0, t \in]0, T[\}$ where the problem is defined. This problem consists of finding a displacement field $\boldsymbol{u} : \boldsymbol{\mathcal{D}} \to \mathbb{R}^d$ and a PK2 stress tensor field $\boldsymbol{S} : \boldsymbol{\mathcal{D}} \to \mathbb{R}^d \otimes \mathbb{R}^d$ such that

$$\rho_0 \frac{\partial^2 u_a}{\partial t^2} - \frac{\partial}{\partial X_A}\{F_{aB} S_{BA}\} = \rho_0 b_a \quad \text{in } \Omega_0 \times]0, T[\,, \quad a = 1, \dots, d, \tag{3.7}$$

$$S_{AB} - 2\frac{\partial \Psi}{\partial C_{AB}} = 0 \qquad \text{in } \Omega_0 \times]0, T[\,, \quad A, B = 1, \dots, d, \tag{3.8}$$

where initial conditions for displacements $\boldsymbol{u}|_{t=0} = \boldsymbol{u}_0$ and velocities $\frac{\partial \boldsymbol{u}}{\partial t}\big|_{t=0} = \dot{\boldsymbol{u}}_0$ in Ω_0 must be prescribed along with proper boundary conditions:

$$\boldsymbol{u} = \boldsymbol{u}_D \quad \text{on } \Gamma_{0,D}, \tag{3.9}$$

$$\boldsymbol{n}_0 \cdot (\boldsymbol{F} \cdot \boldsymbol{S}) = \boldsymbol{t}_N \quad \text{on } \Gamma_{0,N}, \tag{3.10}$$

for the reference configuration Dirichlet $\Gamma_{0,D}$ and Neumann $\Gamma_{0,N}$ boundaries, where prescribed displacements $\boldsymbol{u}_D$ and prescribed tractions $\boldsymbol{t}_N$ are imposed, considering the outward unit vector $\boldsymbol{n}_0$ normal to the reference configuration boundary.

3.4. Variational form of the problem

Let $H^1(\Omega)$ be the space of functions in $L^2(\Omega)$ whose derivatives belong to $L^2(\Omega)$. Consider the field spaces $\mathbb{V} \subset H^1(\Omega)^d$ and $\mathbb{T} \subset L^2(\Omega)^{d \times d}$ where the displacements and the PK2 stresses are well-defined, respectively, for all time $t \in]0, T[$. The subspace $\mathbb{V}_0$ of $\mathbb{V}$ consists of functions $\mathbb{V}$ that vanish on the Dirichlet boundary $\Gamma_{0,D}$. Let $\mathbb{W} = \mathbb{V} \times \mathbb{T}$ and $\mathbb{W}_0 = \mathbb{V}_0 \times \mathbb{T}$ be the spaces where the weak form of the problem is defined, so that the spaces of unknowns $\boldsymbol{U} = [\boldsymbol{u}, \boldsymbol{S}]^T$ and test functions $\boldsymbol{V} = [\boldsymbol{v}, \boldsymbol{T}]^T$ correspond to $\boldsymbol{U} \in \mathbb{W}$ and $\boldsymbol{V} \in \mathbb{W}_0$, respectively.

Let us denote by $\langle \cdot, \cdot \rangle$ the integral of the product of two functions in Ω_0. The variational form of the problem is constructed by testing the system (3.7)-(3.8) against arbitrary test functions $\boldsymbol{V}$. Consequently, the weak form of the problem consists of finding $\boldsymbol{U} :]0, T[\to \mathbb{W}$ such that the initial and boundary conditions are satisfied and

$$\left\langle v_a, \rho_0 \frac{\partial^2 u_a}{\partial t^2} \right\rangle + \mathcal{A}(\boldsymbol{V}, \boldsymbol{U}) = \mathcal{F}(\boldsymbol{V}) \quad \forall \boldsymbol{V} \in \mathbb{W}_0, \tag{3.11}$$

where $\mathcal{A}(\boldsymbol{V}, \boldsymbol{U})$ is a semilinear form defined on $\mathbb{W}_0 \times \mathbb{W}$ as

$$\mathcal{A}(\boldsymbol{V}, \boldsymbol{U}) := \left\langle \frac{\partial v_a}{\partial X_A}, F_{aB} S_{AB} \right\rangle + \langle T_{AB}, S_{AB} \rangle - \left\langle T_{AB}, 2\frac{\partial \Psi}{\partial C_{AB}} \right\rangle, \tag{3.12}$$

and $\mathcal{F}(\boldsymbol{V})$ is a linear form on $\mathbb{W}_0$ defined by

$$\mathcal{F}(\boldsymbol{V}) := \langle v_a, \rho_0 b_a \rangle + \langle v_a, t_{N_a} \rangle_{\Gamma_{0,N}}. \tag{3.13}$$

4. Time integration and linearization

4.1. Time integration

Terms involving time derivatives can be approximated using different approaches, being the finite difference method the most commonly used. In the present work, only implicit time integration is considered because an explicit scheme would require extremely small time steps to fulfil the stability conditions. In the current problem, the second time derivative of the displacement $\frac{\partial^2 \boldsymbol{u}}{\partial t^2} =: \boldsymbol{a}$ has to be approximated at a given time step $t^{n+1} = t^n + \delta t$, where n is the time step counter and δt is the time step size of the uniform partition of the time interval $]0, T[$. In

what follows, only Backward Differentiation Formula (BDF) time integration schemes are considered, and depending on the desired accuracy, the following can be selected:

$$\text{BDF1}: \qquad \boldsymbol{a}^{n+1} = \frac{1}{\delta t^2}\left[\boldsymbol{u}^{n+1} - 2\boldsymbol{u}^{n} + \boldsymbol{u}^{n-1}\right] + \mathcal{O}(\delta t), \tag{4.1}$$

$$\text{BDF2}: \qquad \boldsymbol{a}^{n+1} = \frac{1}{\delta t^2}\left[2\boldsymbol{u}^{n+1} - 5\boldsymbol{u}^{n} + 4\boldsymbol{u}^{n-1} - \boldsymbol{u}^{n-1}\right] + \mathcal{O}(\delta t^2), \tag{4.2}$$

where $\mathcal{O}(\cdot)$ is the approximation order of the scheme depending on the time step size.

4.2. Linearization

The finite strain solid mechanics problem is inherently non-linear, hence it must be linearized in order to solve the system. The idea is to obtain a bilinear operator that allows to compute a correction $\delta\boldsymbol{U} := [\delta\boldsymbol{u}, \delta\boldsymbol{S}]^T$ of the guessed solution $\boldsymbol{U}^{n+1}$ at a time t^{n+1}. The linearization is performed using a Newton-Raphson scheme on the formulation presented in Eq. (3.11), and the unknown becomes the correction of the displacement. Therefore the new problem consists in finding $\delta\boldsymbol{U} \in \mathbb{W}_0$ such that

$$\left\langle \boldsymbol{v}, \rho_0 \frac{C}{\delta t^2}\delta\boldsymbol{u} \right\rangle + \mathcal{B}\left(\boldsymbol{V}, \delta\boldsymbol{U}\right) = \mathcal{F}\left(\boldsymbol{V}\right) - \mathcal{A}\left(\boldsymbol{V}, \boldsymbol{U}^{n+1}\right) - \left\langle \boldsymbol{v}, \rho_0 \boldsymbol{a}^{n+1} \right\rangle \quad \forall \boldsymbol{V} \in \mathbb{W}_0, \tag{4.3}$$

where $\mathcal{B}\left(\boldsymbol{V}, \delta\boldsymbol{U}\right)$ defined on $\mathbb{W}_0 \times \mathbb{W}_0$ is the bilinear form obtained through the linearization of $\mathcal{A}\left(\boldsymbol{V}, \boldsymbol{U}\right)$, and it is defined as

$$\mathcal{B}\left(\boldsymbol{V}, \delta\boldsymbol{U}\right) = \left\langle \frac{\partial v_a}{\partial X_A}, \frac{\partial \delta u_a}{\partial X_B} S_{BA} \right\rangle + \left\langle \frac{\partial v_a}{\partial X_A}, F_{aB}\delta S_{BA} \right\rangle + \left\langle T_{AB}, \delta S_{AB} \right\rangle - \left\langle T_{AB}, \mathbb{C}_{ABCD} F_{aC} \frac{\partial \delta u_a}{\partial X_D} \right\rangle, \tag{4.4}$$

where $\mathbb{C}_{ABCD} = 2\frac{\partial^2 \Psi}{\partial C_{AB} \partial C_{CD}}$ is the constitutive tangent matrix which relates variations of the PK2 stress tensor $\delta\boldsymbol{S}$ and the Right Cauchy tensor $\delta\boldsymbol{C}$. In the same manner, the time derivative term has been linearized as

$$\left.\frac{\partial^2 \boldsymbol{u}}{\partial t^2}\right|_{t^{n+1}} = \frac{C}{\delta t^2}\delta\boldsymbol{u} + \boldsymbol{a}^{n+1}, \tag{4.5}$$

where C is a coefficient that depends on the integration scheme; precisely $C = 1$ for BDF1 and $C = 2$ for BDF2, and $\boldsymbol{a}^{n+1}$ is the acceleration obtained in the previous iteration, computed as stated in Eqs. (4.1) and (4.2).

Note that the bilinear formm $\mathcal{B}$ depends on the unknown of the previous iteration $\boldsymbol{U}^{n+1}$ through the evaluation of the different tensor functions that depend on it, even though this dependence has not been explicitly displayed.

4.3. Symmetrization

The symmetric form of the problem can be obtained from Eq. (4.3) by multiplying the linearized terms of the constitutive equation by $-\mathbb{C}^{-1}$, resulting in

$$\left\langle \boldsymbol{v}, \rho_0 \frac{C}{\delta t^2}\delta\boldsymbol{u} \right\rangle + \mathcal{B}^{\text{sym}}\left(\boldsymbol{V}, \delta\boldsymbol{U}\right) = \mathcal{F}\left(\boldsymbol{V}\right) - \mathcal{A}^{\text{sym}}\left(\boldsymbol{V}, \boldsymbol{U}^{n+1}\right) - \left\langle \boldsymbol{v}, \rho_0 \boldsymbol{a}^{n+1} \right\rangle \quad \forall \boldsymbol{V} \in \mathbb{W}_0, \tag{4.6}$$

where

$$\mathcal{B}^{\text{sym}}\left(\boldsymbol{V}, \delta\boldsymbol{U}\right) = \left\langle \frac{\partial v_a}{\partial X_A}, \frac{\partial \delta u_a}{\partial X_B} S_{BA} \right\rangle + \left\langle \frac{\partial v_a}{\partial X_A}, F_{aB}\delta S_{BA} \right\rangle - \left\langle T_{AB}, \mathbb{C}^{-1}_{ABCD}\delta S_{CD} \right\rangle + \left\langle T_{AB}, F_{aA}\frac{\partial \delta u_a}{\partial X_B} \right\rangle, \tag{4.7}$$

$$\mathcal{A}^{\text{sym}}(\boldsymbol{V}, \boldsymbol{U}) = \left\langle \frac{\partial v_a}{\partial X_A}, F_{aB}S_{AB} \right\rangle - \left\langle T_{AB}, \mathbb{C}^{-1}_{ABCD}S_{CD} \right\rangle + \left\langle T_{AB}, 2\mathbb{C}^{-1}_{ABCD}\frac{\partial \Psi}{\partial C_{CD}} \right\rangle. \tag{4.8}$$

By utilizing the symmetric form of the problem, we tackle an energy minimization problem, employing stresses as test functions instead of strains found in the non-symmetric form. This approach offers computational advantages, allowing to use solvers particularly adapted to symmetric systems of equations. However, to simplify the exposition we will consider next the FE approximation to Eq. (4.3).

5. Finite element approximation

5.1. Galerkin finite element formulation

The standard Galerkin approximation of the variational problem defined in Eq. (4.3) can be constructed by taking a FE partition $\mathcal{P}_h$ of the domain Ω_0 corresponding to the solid-shell and constructed using the extrusion described in Section 2. The diameter of an element domain $K \in \mathcal{T}_h$ is denoted by h_K, and the diameter of the element partition is defined as $h = \max\{h_K | K \in \mathcal{P}_h\}$. Under the considerations above, the conforming FE spaces are constructed in the usual manner $\mathbb{V}_h \subset \mathbb{V}$ and $\mathbb{T}_h \subset \mathbb{T}$; therefore $\mathbb{W}_h = \mathbb{V}_h \times \mathbb{T}_h$. The subspace of $\mathbb{V}_h$ of vectors that vanish on the Dirichlet boundary is denoted as $\mathbb{V}_{h,0} \subset \mathbb{V}_0$, and $\mathbb{W}_{h,0} = \mathbb{V}_{h,0} \times \mathbb{T}_h$.

The Galerkin FE approximation consists of finding $\delta \boldsymbol{U}_h = [\delta \boldsymbol{u}_h, \delta \boldsymbol{S}_h]^T \in \mathbb{W}_{h,0}$ for a time t^{n+1} in a given iteration, such that

$$\left\langle \boldsymbol{v}_h, \rho_0 \frac{C}{\delta t^2} \delta \boldsymbol{u}_h \right\rangle + \mathcal{B}\left(\boldsymbol{V}_h, \delta \boldsymbol{U}_h\right) = \mathcal{F}\left(\boldsymbol{V}_h\right) - \mathcal{A}\left(\boldsymbol{V}_h, \boldsymbol{U}_h^{n+1}\right) - \left\langle \boldsymbol{v}_h, \rho_0 \boldsymbol{a}_h^{n+1} \right\rangle \quad \forall \boldsymbol{V}_h \in \mathbb{W}_{h,0}. \tag{5.1}$$

The Galerkin FE approximation lacks of stability unless particular interpolations are used to interpolate the displacement and PK2 stress fields, requiring to satisfy appropriate inf-sup conditions [16]. Let us consider now the symmetrized problem (4.6) and discuss the stability of this linearized problem, although the discussion could be extended to the original nonlinear problem. Taking $\boldsymbol{v}_h = \delta \boldsymbol{u}_h$ (assuming homogeneous Dirichlet boundary conditions) and $\boldsymbol{T}_h = -\delta \boldsymbol{S}_h$ it is found that

$$\mathcal{B}^{\mathrm{sym}}\left(\boldsymbol{V}_h, \delta \boldsymbol{U}_h\right) = \left\langle \frac{\partial \delta u_{h,a}}{\partial X_A}, \frac{\partial \delta u_{h,a}}{\partial X_B} S_{h,BA} \right\rangle + \left\langle \delta S_{h,AB}, \mathbb{C}^{-1}_{ABCD} \delta S_{h,CD} \right\rangle.$$

Suppose that the given guess is away from buckling, so that the solution of the continuous problem exists and is unique. Since, for thermodynamical reasons, $\mathbb{C}^{-1}$ is known to be a positive-definite tensor, the second term defines a norm of tensor $\delta \boldsymbol{S}_h$ and thus one can have control on this norm. However, it is obvious that $\boldsymbol{S}_h$ is not positive-definite, and therefore the first term can be either positive or negative. The only possibility to have control on the displacement gradients is to satisfy the inf-sup condition

$$\inf_{\boldsymbol{v}_h \in \mathbb{V}_{0,h}} \sup_{\boldsymbol{T}_h \in \mathbb{T}_h} \frac{\langle \nabla \boldsymbol{v}_h, \boldsymbol{T}_h \rangle}{\|\boldsymbol{v}_h\|_{\mathbb{W}} \|\boldsymbol{T}_h\|_{\mathbb{T}}} \geqslant \beta_1, \tag{5.2}$$

for a constant $\beta_1 > 0$. This, in turn, guarantees that the global inf-sup condition of the problem, which can be written as

$$\inf_{\delta \boldsymbol{U}_h \in \mathbb{W}_{0,h}} \sup_{\boldsymbol{V}_h \in \mathbb{W}_h} \frac{\mathcal{B}^{\mathrm{sym}}\left(\boldsymbol{V}_h, \delta \boldsymbol{U}_h\right)}{\|\boldsymbol{V}_h\|_{\mathbb{W}} \|\delta \boldsymbol{U}_h\|_{\mathbb{W}}} \geqslant \beta_2,$$

will be satisfied for a constant $\beta_2 > 0$. However, FE element interpolations satisfying the compatibility condition (5.2) are rare and difficult to implement. In particular, it is not satisfied by the convenient equal interpolation for displacements and stresses. However, the need to satisfy condition (5.2) to obtain a stable formulation is circumvented if stabilized FE formulations are used. We present one of these formulations in the next subsection.

5.2. Stabilized finite element formulation

The stabilized formulation employed in the present work follows the VMS framework, first proposed by Hughes et al. [18]. The idea is to add additional consistent terms to the original Galerkin FE formulation that enhance the stability without upsetting the accuracy. In this case, this is achieved by adding a finer resolution space $\bar{\mathbb{W}}$, called sub-grid scale (SGS) space, to the FE space $\mathbb{W}_h$. Therefore, the space in which the problem is defined is split into two parts, $\mathbb{W} = \mathbb{W}_h \oplus \bar{\mathbb{W}}$, implying that $\mathbb{V} = \mathbb{V}_h \oplus \bar{\mathbb{V}}$ and $\mathbb{T} = \mathbb{T}_h \oplus \bar{\mathbb{T}}$. In the same manner, the space $\mathbb{W}_0$ is split as $\mathbb{W}_0 = \mathbb{W}_{h,0} \oplus \bar{\mathbb{W}}_0$. As a consequence the unknowns are split into $\boldsymbol{U} = \boldsymbol{U}_h + \bar{\boldsymbol{U}}$, where $\bar{\boldsymbol{U}} = \left[\bar{\boldsymbol{u}}, \bar{\boldsymbol{S}}\right]^T \in \bar{\mathbb{W}}_0$ is the SGS. The same split applies to the iterative increments, $\delta \boldsymbol{U} = \delta \boldsymbol{U}_h + \delta \bar{\boldsymbol{U}}$.

With the splitting introduced, problem in (5.1) turns into: find $\delta \boldsymbol{U} \in \mathbb{W}_{h,0}$ and $\bar{\boldsymbol{U}} \in \bar{\mathbb{W}}_0$ such that

$$\left\langle \boldsymbol{v}_h, \rho_0 \frac{C}{\delta t^2} \delta \boldsymbol{u}_h \right\rangle + \left\langle \boldsymbol{v}_h, \rho_0 \bar{\boldsymbol{a}}^{n+1} \right\rangle + \mathcal{B}\left(\boldsymbol{V}_h, \delta \boldsymbol{U}_h\right) + \mathcal{B}\left(\boldsymbol{V}_h, \delta \bar{\boldsymbol{U}}\right) = \mathcal{F}\left(\boldsymbol{V}_h\right) - \mathcal{A}\left(\boldsymbol{V}_h, \boldsymbol{U}_h^{n+1} + \bar{\boldsymbol{U}}^{n+1}\right) - \left\langle \boldsymbol{v}_h, \rho_0 \boldsymbol{a}_h^{n+1} \right\rangle,$$

$$\left\langle \bar{\boldsymbol{v}}, \rho_0 \frac{C}{\delta t^2} \delta \boldsymbol{u}_h \right\rangle + \left\langle \bar{\boldsymbol{v}}, \rho_0 \bar{\boldsymbol{a}}^{n+1} \right\rangle + \mathcal{B}\left(\bar{\boldsymbol{V}}, \delta \boldsymbol{U}_h\right) + \mathcal{B}\left(\bar{\boldsymbol{V}}, \delta \bar{\boldsymbol{U}}\right) = \mathcal{F}\left(\bar{\boldsymbol{V}}\right) - \mathcal{A}\left(\bar{\boldsymbol{V}}, \boldsymbol{U}_h^{n+1} + \bar{\boldsymbol{U}}^{n+1}\right) - \left\langle \bar{\boldsymbol{v}}, \rho_0 \boldsymbol{a}_h^{n+1} \right\rangle,$$

for all $\boldsymbol{V}_h \in \mathbb{W}_{h,0}$ and $\bar{\boldsymbol{V}} \in \bar{\mathbb{W}}_0$. Since $\bar{\boldsymbol{U}}^{n+1}$ is expected to be small, we may approximate

$$\mathcal{A}\left(\bar{\boldsymbol{V}}, \boldsymbol{U}_h^{n+1} + \bar{\boldsymbol{U}}^{n+1}\right) \approx \mathcal{A}\left(\bar{\boldsymbol{V}}, \boldsymbol{U}_h^{n+1}\right) + \mathcal{B}\left(\bar{\boldsymbol{V}}, \bar{\boldsymbol{U}}\right),$$

and arrive to the problem:

$$\left\langle \boldsymbol{v}_h, \rho_0 \frac{C}{\delta t^2} \delta \boldsymbol{u}_h \right\rangle + \left\langle \boldsymbol{v}_h, \rho_0 \bar{\boldsymbol{a}}^{n+1} \right\rangle + \mathcal{B}\left(\boldsymbol{V}_h, \delta \boldsymbol{U}_h\right) + \mathcal{B}\left(\boldsymbol{V}_h, \bar{\boldsymbol{U}}\right) = \mathcal{F}\left(\boldsymbol{V}_h\right) - \mathcal{A}\left(\boldsymbol{V}_h, \boldsymbol{U}_h^{n+1}\right) - \left\langle \boldsymbol{v}_h, \rho_0 \boldsymbol{a}_h^{n+1} \right\rangle, \tag{5.3}$$

$$\left\langle \bar{\boldsymbol{v}}, \rho_0 \frac{C}{\delta t^2} \delta \boldsymbol{u}_h \right\rangle + \left\langle \bar{\boldsymbol{v}}, \rho_0 \bar{\boldsymbol{a}}^{n+1} \right\rangle + \mathcal{B}\left(\bar{\boldsymbol{V}}, \delta \boldsymbol{U}_h\right) + \mathcal{B}\left(\bar{\boldsymbol{V}}, \bar{\boldsymbol{U}}\right) = \mathcal{F}\left(\bar{\boldsymbol{V}}\right) - \mathcal{A}\left(\bar{\boldsymbol{V}}, \boldsymbol{U}_h^{n+1}\right) - \left\langle \bar{\boldsymbol{v}}, \rho_0 \boldsymbol{a}_h^{n+1} \right\rangle, \tag{5.4}$$

Here, Eq. (5.3) is called FE equation and Eq. (5.4) is called SGS equation. Note that we need to approximate for the SGS, not only for its iterative increment.

The main idea to derive the stabilized FE formulation is to obtain an expression for the SGS $\bar{\boldsymbol{U}}$ in terms of the FE variables from the SGS equation. For this matter, consider that the SGSs behave as bubble functions, whose velocity components vanish at the inter-element boundaries, although this assumption can be relaxed [29]. Therefore, Eq. (5.4) can be integrated by parts within each element to obtain

$$\begin{aligned} \sum_K \left\langle \bar{\boldsymbol{v}}_h, \rho_0 \frac{C}{\delta t^2} \delta \boldsymbol{u}_h \right\rangle_K + \sum_K \left\langle \bar{\boldsymbol{v}}, \rho_0 \bar{\boldsymbol{a}}^{n+1} \right\rangle_K + \sum_K \left\langle \bar{\boldsymbol{V}}, \mathrm{B}\left(\delta \boldsymbol{U}_h\right) \right\rangle_K + \sum_K \left\langle \bar{\boldsymbol{V}}, \mathrm{B}\left(\bar{\boldsymbol{U}}\right) \right\rangle_K \\ = \sum_K \left\langle \bar{\boldsymbol{V}}, \mathrm{F} \right\rangle_K - \sum_K \left\langle \bar{\boldsymbol{V}}, \mathrm{A}\left(\boldsymbol{U}_h^{n+1}\right) \right\rangle_K - \sum_K \left\langle \bar{\boldsymbol{v}}, \rho_0 \boldsymbol{a}_h^{n+1} \right\rangle_K, \end{aligned} \tag{5.5}$$

for all $\bar{\boldsymbol{V}} \in \bar{\mathbb{W}}$, where the operators $\mathrm{B} = [\mathrm{B}_u, \mathrm{B}_S]^T$ and $\mathrm{A} = [\mathrm{A}_u, \mathrm{A}_S]^T$ which come from integration by parts $\mathcal{B}\left(\bar{\boldsymbol{V}}, \delta \boldsymbol{U}_h\right) = \sum_K \left\langle \bar{\boldsymbol{V}}, \mathrm{B}\left(\delta \boldsymbol{U}_h\right) \right\rangle_K$ and $\mathcal{A}\left(\bar{\boldsymbol{V}}, \delta \boldsymbol{U}_h\right) = \sum_K \left\langle \bar{\boldsymbol{V}}, \mathrm{A}\left(\delta \boldsymbol{U}_h\right) \right\rangle_K$, respectively, and $\mathrm{F} = [\mathrm{F}_u, \mathrm{F}_S]^T$ are defined by

$$\mathrm{B}_u\left(\delta \boldsymbol{U}_h\right)_a = -\frac{\partial}{\partial X_A}\left\{\frac{\delta u_{h_a}}{\partial X_B} S_{AB}\right\} - \frac{\partial}{\partial X_A}\left\{F_{aB} \delta S_{h_{AB}}\right\}, \tag{5.6}$$

$$\mathrm{B}_S\left(\delta \boldsymbol{U}_h\right)_{AB} = \delta S_{h_{AB}} - \mathbb{C}_{ABCD} F_{aC} \frac{\partial \delta u_{h_a}}{\partial X_D}, \tag{5.7}$$

$$\mathrm{A}_u\left(\boldsymbol{U}_h^{n+1}\right)_a = -\frac{\partial}{\partial X_A}\left\{F_{aB} S_{BA}\right\}, \tag{5.8}$$

$$\mathrm{A}_S\left(\boldsymbol{U}_h^{n+1}\right)_{AB} = S_{AB} - 2\frac{\partial \Psi}{\partial C_{AB}}, \tag{5.9}$$

$$\mathrm{F}_u = \rho_0 b_a, \tag{5.10}$$

$$\mathrm{F}_S = 0. \tag{5.11}$$

Let us consider the SGSs to be quasi-static, implying that the time derivative terms of the SGS are neglected. Then, Eq. (5.5) enforces that

$$\bar{\Pi}\left(\mathrm{B}\left(\delta \boldsymbol{U}_h\right) + \mathrm{B}\left(\bar{\boldsymbol{U}}\right)\right) = \bar{\Pi}\left(\mathrm{F} - \mathrm{A}\left(\boldsymbol{U}_h^{n+1}\right)\right), \tag{5.12}$$

where $\bar{\Pi}$ is the $L^2\left(\Omega_0\right)$ projection into the SGS space. Let us define the following residual operators

$$\begin{aligned} \mathrm{R}_{\delta \boldsymbol{U}}\left(\delta \boldsymbol{U}_h\right) &= -\mathrm{B}\left(\delta \boldsymbol{U}_h\right), \\ \mathrm{R}_{\boldsymbol{U}}\left(\boldsymbol{U}_h^{n+1}\right) &= \mathrm{F} - \mathrm{A}\left(\boldsymbol{U}_h^{n+1}\right). \end{aligned}$$

An expression for the SGS can be obtained from Eq. (5.4) in the form of

$$\bar{\Pi}\left(\boldsymbol{\tau}_K^{-1} \bar{\boldsymbol{U}}\right) = \bar{\Pi}\left(\mathrm{R}_{\delta \boldsymbol{U}}\left(\delta \boldsymbol{U}_h\right) + \mathrm{R}_{\boldsymbol{U}}\left(\boldsymbol{U}_h^{n+1}\right)\right), \tag{5.13}$$

where the matrix $\boldsymbol{\tau}_K^{-1}$ is an approximation of the operator B withing each element K. The details on how to design $\boldsymbol{\tau}_K$ are not discussed in the present work, but can be reviewed in [30, 31]. In this case, $\boldsymbol{\tau}_K$ is taken as a diagonal matrix where the stabilization parameters are taken from [32, 33] as the following

$$\boldsymbol{\tau}_K = \begin{bmatrix} \tau_u \boldsymbol{I}_d & \boldsymbol{0} \\ \boldsymbol{0} & \tau_S \boldsymbol{I} \end{bmatrix}, \qquad \tau_u = c_u \frac{h_K^2}{2\mu}, \qquad \tau_S = c_S,$$

where c_u and c_S are algorithmic parameters to be chosen. Considering that $\boldsymbol{\tau}_K^{-1}\bar{\boldsymbol{U}}$ belongs to the SGS space, the projection results in the identity $\bar{\Pi}\left(\boldsymbol{\tau}_K^{-1}\bar{\boldsymbol{U}}\right) = \boldsymbol{\tau}_K^{-1}\bar{\boldsymbol{U}}$. Therefore, an expression of the SGS can be obtained in terms of the FE variables from Eq. (5.13) as

$$\bar{\boldsymbol{U}} \approx \boldsymbol{\tau}_K \bar{\Pi}\left(\mathrm{R}_{\delta\boldsymbol{U}}\left(\delta\boldsymbol{U}_h\right) + \mathrm{R}_{\boldsymbol{U}}\left(\boldsymbol{U}_h^{n+1}\right)\right) \qquad \text{in } K \in \mathcal{P}_h.$$

The SGS can now be introduced in Eq. (5.3), and the new stabilized form of the problem reads

$$\begin{aligned}\left\langle \boldsymbol{v}_h, \rho_0 \frac{C}{\delta t^2}\delta\boldsymbol{u}_h \right\rangle + \left\langle \boldsymbol{v}_h, \rho_0 \bar{\boldsymbol{a}}^{n+1} \right\rangle + \mathcal{B}\left(\boldsymbol{V}_h, \delta\boldsymbol{U}_h\right) + \sum_K \boldsymbol{\tau}_K \left\langle \mathrm{L}\left(\boldsymbol{V}_h\right), \bar{\Pi}\left(\mathrm{R}_{\delta\boldsymbol{U}}\left(\delta\boldsymbol{U}_h\right)\right)\right\rangle_K \\ = \mathcal{F}\left(\boldsymbol{V}_h\right) - \mathcal{A}\left(\boldsymbol{V}_h, \boldsymbol{U}_h^{n+1}\right) - \left\langle \boldsymbol{v}_h, \rho_0 \boldsymbol{a}_h^{n+1} \right\rangle - \sum_K \boldsymbol{\tau}_K \left\langle \mathrm{L}\left(\boldsymbol{V}_h\right), \bar{\Pi}\left(\mathrm{R}_{\boldsymbol{U}}\left(\boldsymbol{U}_h^{n+1}\right)\right)\right\rangle_K, \end{aligned} \tag{5.14}$$

where $\mathrm{L}\left(\boldsymbol{V}_h\right) = \left[\mathrm{L}_u\left(\boldsymbol{V}_h\right), \mathrm{L}_S\left(\boldsymbol{V}_h\right)\right]^T$ comes from the integration by parts $\mathcal{B}\left(\boldsymbol{V}_h, \bar{\boldsymbol{U}}\right) = \sum_K \left\langle \mathrm{L}\left(\boldsymbol{V}_h\right), \bar{\boldsymbol{U}}\right\rangle_K$, whose components are defined by

$$\mathrm{L}_u\left(\boldsymbol{V}_h\right)_a = -\frac{\partial}{\partial X_B}\left\{\frac{\partial v_a}{\partial X_A} S_{BA}\right\} + \frac{\partial}{\partial X_D}\left\{T_{AB}\mathbb{C}_{ABCD}F_{aC}\right\} \tag{5.15}$$

$$\mathrm{L}_S\left(\boldsymbol{V}_h\right)_{AB} = \frac{\partial v_a}{\partial X_A}F_{aB} + T_{AB} \tag{5.16}$$

From this point, it only remains to choose to which space the SGSs belong. In the VMS framework, there are several possibilities, which can be revised in a general extent in [34, 35, 20, 21]. In a practical sense, it determines the type of projection performed by $\bar{\Pi}$. In what follows, three possibilities are presented.

5.2.1. Algebraic Sub-Grid Scales (ASGS)

The simplest choice is to consider the projection as the identity on the residuals as $\bar{\Pi} = I$ in each element K. Thus, we have that

$$\bar{\Pi}\left(\mathrm{R}_{\delta\boldsymbol{U}}\left(\delta\boldsymbol{U}_h\right) + \mathrm{R}_{\boldsymbol{U}}\left(\boldsymbol{U}_h^{n+1}\right)\right) = \mathrm{R}_{\delta\boldsymbol{U}}\left(\delta\boldsymbol{U}_h\right) + \mathrm{R}_{\boldsymbol{U}}\left(\boldsymbol{U}_h^{n+1}\right), \tag{5.17}$$

and the stabilized formulation (5.14) becomes

$$\begin{aligned}\left\langle \boldsymbol{v}_h, \rho_0 \frac{C}{\delta t^2}\delta\boldsymbol{u}_h \right\rangle + \left\langle \boldsymbol{v}_h, \rho_0 \bar{\boldsymbol{a}}^{n+1} \right\rangle + \mathcal{B}\left(\boldsymbol{V}_h, \delta\boldsymbol{U}_h\right) + \sum_K \boldsymbol{\tau}_K \left\langle \mathrm{L}\left(\boldsymbol{V}_h\right), \mathrm{R}_{\delta\boldsymbol{U}}\left(\delta\boldsymbol{U}_h\right)\right\rangle_K \\ = \mathcal{F}\left(\boldsymbol{V}_h\right) - \mathcal{A}\left(\boldsymbol{V}_h, \boldsymbol{U}_h^{n+1}\right) - \left\langle \boldsymbol{v}_h, \rho_0 \boldsymbol{a}_h^{n+1} \right\rangle - \sum_K \boldsymbol{\tau}_K \left\langle \mathrm{L}\left(\boldsymbol{V}_h\right), \mathrm{R}_{\boldsymbol{U}}\left(\boldsymbol{U}_h^{n+1}\right)\right\rangle_K. \end{aligned} \tag{5.18}$$

5.2.2. Orthogonal Sub-Grid Scales (OSGS)

The most natural approach would be to choose the SGS space to be the orthogonal complement to the FE space. Therefore the projection can be computed as the identity minus the FE part of the residual as $\bar{\Pi} = I - \Pi^h$, where Π^h is the $L^2\left(\Omega_0\right)$ projection into the FE space. Thus, in this case we have:

$$\bar{\Pi}\left(\mathrm{R}_{\delta\boldsymbol{U}}\left(\delta\boldsymbol{U}_h\right) + \mathrm{R}_{\boldsymbol{U}}\left(\boldsymbol{U}_h^{n+1}\right)\right) = \mathrm{R}_{\delta\boldsymbol{U}}\left(\delta\boldsymbol{U}_h\right) + \mathrm{R}_{\boldsymbol{U}}\left(\boldsymbol{U}_h^{n+1}\right) - \Pi^h\left(\mathrm{R}_{\boldsymbol{U}}\left(\boldsymbol{U}_h^{n+1}\right)\right),$$

and the stabilized formulation (5.14) becomes

$$\begin{aligned}\left\langle \boldsymbol{v}_h, \rho_0 \frac{C}{\delta t^2}\delta\boldsymbol{u}_h \right\rangle + \left\langle \boldsymbol{v}_h, \rho_0 \bar{\boldsymbol{a}}^{n+1} \right\rangle + \mathcal{B}\left(\boldsymbol{V}_h, \delta\boldsymbol{U}_h\right) + \sum_K \boldsymbol{\tau}_K \left\langle \mathrm{L}\left(\boldsymbol{V}_h\right), \mathrm{R}_{\delta\boldsymbol{U}}\left(\delta\boldsymbol{U}_h\right)\right\rangle_K \\ = \mathcal{F}\left(\boldsymbol{V}_h\right) - \mathcal{A}\left(\boldsymbol{V}_h, \boldsymbol{U}_h^{n+1}\right) - \left\langle \boldsymbol{v}_h, \rho_0 \boldsymbol{a}_h^{n+1} \right\rangle - \sum_K \boldsymbol{\tau}_K \left\langle \mathrm{L}\left(\boldsymbol{V}_h\right), \mathrm{R}_{\boldsymbol{U}}\left(\boldsymbol{U}_h^{n+1}\right) - \Pi^h\left(\mathrm{R}_{\boldsymbol{U}}\left(\boldsymbol{U}_h^{n+1}\right)\right)\right\rangle_K. \end{aligned} \tag{5.19}$$

5.2.3. Split-Orthogonal Sub-Grid Scales (S-OSGS)

Another possibility is to formulate the OSGS stabilization using the minimum number of terms to stabilize the problem. To achieve this, components of $\mathrm{B}\left(\delta\boldsymbol{U}_h\right)$, $\mathrm{A}\left(\boldsymbol{U}_h^{n+1}\right)$ and $\mathrm{L}\left(\boldsymbol{V}_h\right)$ presented in equations (5.6)-(5.11) and

(5.15)-(5.16) are split into $\mathrm{B}^* = [\mathrm{B}^*_u, \mathrm{B}^*_S]^T$, $\mathrm{A}^* = [\mathrm{A}^*_u, \mathrm{A}^*_S]^T$ and $\mathrm{L} = [\mathrm{L}^*_u, \mathrm{L}^*_S]^T$ defined as

$$\begin{aligned}
\mathrm{B}^*_u\left(\delta\boldsymbol{U}_h\right)_a &= 0,\\
\mathrm{B}^*_S\left(\delta\boldsymbol{U}_h\right)_{AB} &= -\mathbb{C}_{ABCD}F_{aC}\frac{\partial\delta u_{h_a}}{\partial X_D},\\
\mathrm{A}^*_u\left(\boldsymbol{U}_h^{n+1}\right)_a &= 0,\\
\mathrm{A}^*_S\left(\boldsymbol{U}_h^{n+1}\right)_{AB} &= -2\frac{\partial\Psi}{\partial C_{AB}},\\
\mathrm{L}^*_u\left(\boldsymbol{V}_h\right)_a &= 0,\\
\mathrm{L}^*_S\left(\boldsymbol{V}_h\right)_{AB} &= \frac{\partial v_a}{\partial X_A}F_{aB}.
\end{aligned}$$

The residual operators are modified accordingly to $\mathrm{R}^*_{\delta\boldsymbol{U}}\left(\delta\boldsymbol{U}_h\right) = -\mathrm{B}^*\left(\delta\boldsymbol{U}_h\right)$ and $\mathrm{R}^*_{\boldsymbol{U}}\left(\boldsymbol{U}_h^{n+1}\right) = \mathrm{F} - \mathrm{A}^*\left(\boldsymbol{U}_h^{n+1}\right)$, and the stabilized S-OSGS formulation results in

$$\begin{aligned}
&\left\langle \boldsymbol{v}_h, \rho_0\frac{C}{\delta t^2}\delta\boldsymbol{u}_h\right\rangle + \left\langle \boldsymbol{v}_h, \rho_0\bar{\boldsymbol{a}}^{n+1}\right\rangle + \mathcal{B}\left(\boldsymbol{V}_h, \delta\boldsymbol{U}_h\right) + \sum_K \boldsymbol{\tau}_K\left\langle \mathrm{L}^*\left(\boldsymbol{V}_h\right), \mathrm{R}^*_{\delta\boldsymbol{U}}\left(\delta\boldsymbol{U}_h\right)\right\rangle_K\\
&\quad = \mathcal{F}\left(\boldsymbol{V}_h\right) - \mathcal{A}\left(\boldsymbol{V}_h, \boldsymbol{U}_h^{n+1}\right) - \left\langle \boldsymbol{v}_h, \rho_0\boldsymbol{a}_h^{n+1}\right\rangle - \sum_K \boldsymbol{\tau}_K\left\langle \mathrm{L}^*\left(\boldsymbol{V}_h\right), \mathrm{R}^*_{\boldsymbol{U}}\left(\boldsymbol{U}_h^{n+1}\right) - \Pi^h\left(\mathrm{R}^*_{\boldsymbol{U}}\left(\boldsymbol{U}_h^{n+1}\right)\right)\right\rangle_K. \qquad (5.20)
\end{aligned}$$

This variation of the OSGS approach is not merely a simplification, since it retains the optimal L^2-convergence rate respect to the element size, but also has improved capabilities in problems with high gradients of the solution.

6. Numerical examples

This section presents a set of numerical examples designed to evaluate the performance of the stabilized FE formulation, considering that it is suitable for both regular solid elements and thin solid-shell elements. In a first instance the order of convergence and accuracy of the solution are assessed using solid elements in 2D and 3D cases, as the stabilized displacement-stress formulation presented has not been proposed before. Subsequently, three shell benchmark problems of different initial curvatures are solved for the numerical locking assessment. In these three shell examples, we have compared two approaches, namely, the irreducible formulation with quadratic elements and the mixed formulation with linear elements across the thickness of the shell. None of them locks, but we have checked that the irreducible formulation with linear elements locks in all cases, and thus results are not included.

6.1. Manufactured solution

The first numerical example is designed to test the proposed formulation to check its order of convergence with respect to the element size h. The case consists of a 2D solid body subjected to a load whose analytical solution is known. To do this, the analytical solution is substituted in the continuum equations to obtain the forcing terms that lead to the deformation state. In this manner, they can be introduced in the discretized FE computations with the corresponding boundary conditions. All the quantities are assumed dimensionless for this example.

The problem consists of a 2D solid under plane strain assumption, the domain is a square $\Omega_0 = (0,1)\times(0,1)$ whose imposed manufactured displacement field is

$$\boldsymbol{u}\left(X,Y\right) = 0.001\left[\exp\left(X+Y\right), \exp\left(X+Y\right)\right], \qquad (6.1)$$

for the Cartesian coordinates X and Y in the reference configuration. The material is set as Neo-Hookean with shear modulus $\mu = 1375000$ and Poisson's ratio $\nu = 0.2$. The PK2 stress tensor field is computed with respect to the manufactured solution as

$$\boldsymbol{S} = \mu\left(\boldsymbol{I} - \boldsymbol{C}^{-1}\right) + \lambda\left(\ln J\right)\boldsymbol{C}^{-1}. \qquad (6.2)$$

The case is computed for different meshes of square bilinear elements, increasing the number of elements per side progressively, and computing the error in the $L^2(\Omega_0)$ error norm. Convergence curves for displacements and PK2 stresses for the ASGS, OSGS and S-OSGS mixed formulations upon mesh refinement are plotted in Fig. 3, and with respect to the total number of degrees of freedom in Fig. 4.

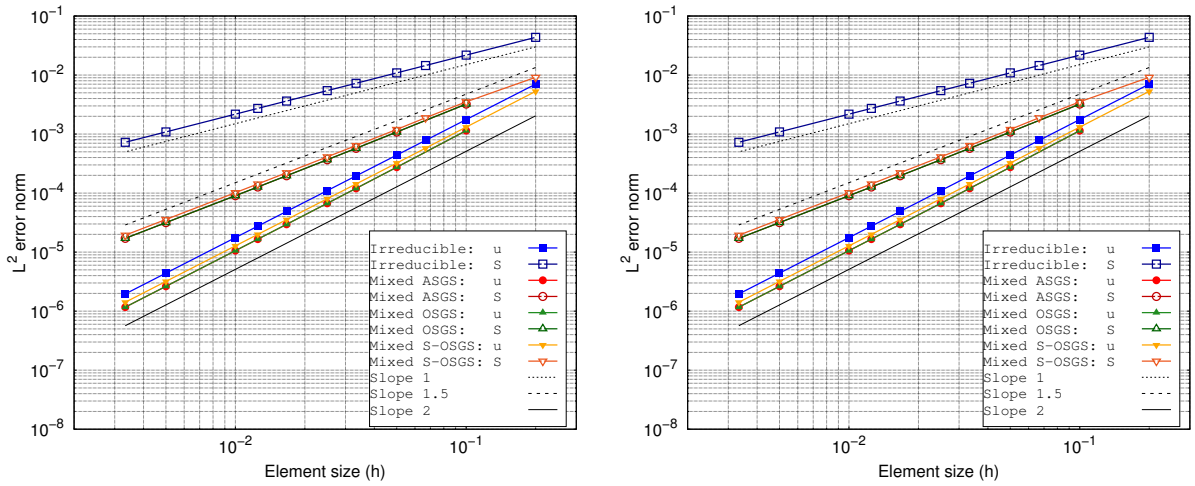

Figure 3: Displacement (left) and PK2 stress (right) convergence curves upon mesh refinement.

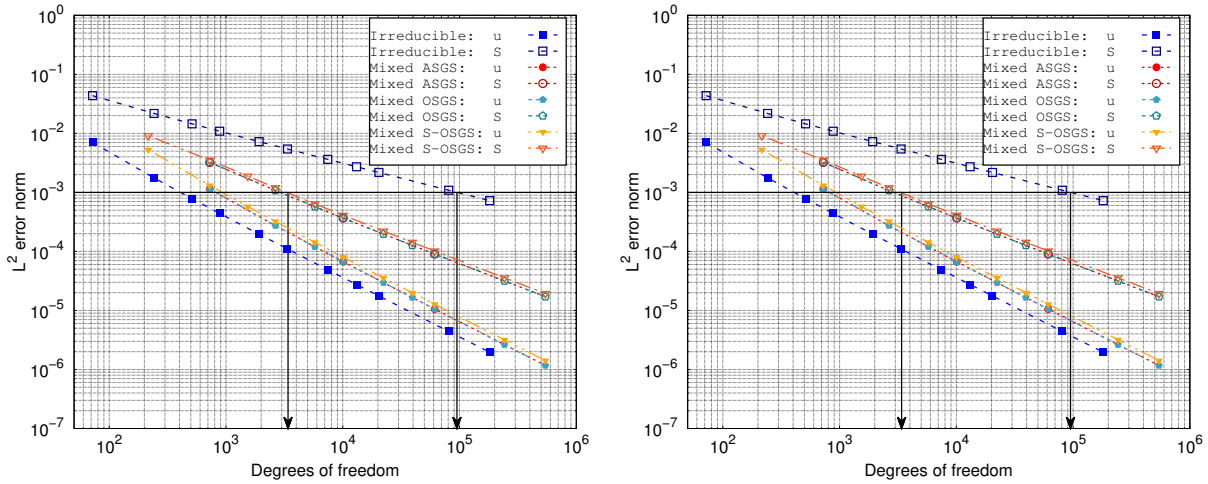

Figure 4: Displacement (left) and PK2 stress (right) convergence curves with respect to the total number of degrees of freedom.

Results in Fig. 3 show that the slope of convergence for displacements are of order 2 in the irreducible and the stabilized mixed formulations, which is theoretically correct. However, PK2 stresses in the stabilized mixed formulation cases show a super-convergence rate of slope 1.5 instead of the theoretical rate of 1, which is the expected for linear interpolation elements. Furthermore, the accuracy of the PK2 stress upon mesh refinement is also greatly increased in the stabilized mixed formulations when compared to the irreducible one since the later requires a mesh nearly 10 times finer to achieve the same degree of error. The increased accuracy can be verified from the results in Fig. 4, where accuracy vs the number of degrees of freedom is compared; this number is what defines the size of the problem. By comparing the $L^2(\Omega_0)$ error norm obtained for each formulation and for each field with respect to the fixed error threshold 10^{-3} shown in the plot, it becomes clear that the accuracy of the PK2 stress field is highly enhanced in the stabilized mixed formulations, at the cost of a slightly diminished accuracy of the displacement field.

6.2. Twisting column

The twisting column is a classical test to assess the robustness of a FE formulation in extreme non-linear deformations [36, 37]. The problem consists of a column of length $L = 6$ m and square transverse shape of side $a = 1$ m whose center aligns with the origin, clamped on the bottom face and subject to an initial velocity defined as

$$\boldsymbol{v}_0\left(X, Y, Z\right) = \omega \sin\left(\frac{\pi Z}{2L}\right)\left(Y, -X, 0\right)^T \qquad \left[\frac{\mathrm{m}}{\mathrm{s}}\right], \tag{6.3}$$

for the angular velocity $\omega = 100$ rad/s and Cartesian coordinates X, Y, Z. The geometry, mesh and boundary conditions are illustrated in Fig. 5. The material is defined as Neo-Hookean, with a Young modulus $E = 1.7 \cdot 10^7$ Pa, a Poisson's ratio $\nu = 0.3$ and an initial density $\rho_0 = 1100$ kg/m^3. Three different meshes are used: Mesh 1 with $10 \times 10 \times 60$, Mesh 2 with $15 \times 15 \times 80$ and Mesh 3 with $20 \times 20 \times 100$ structured trilinear hexahedral elements.

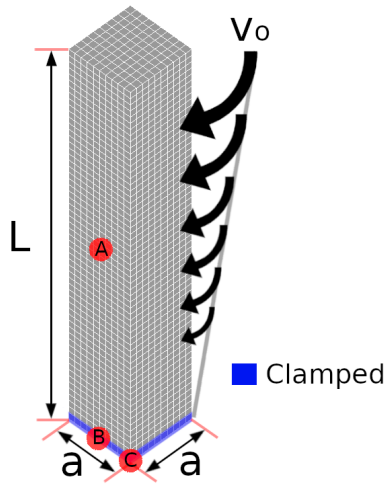

Figure 5: Twisting column: geometry, mesh and boundary conditions.

The problem is run with a BDF2 time integration scheme because it is second order accurate in time and it is also able to dissipate non-physical mode oscillations. It has also been proven in [24] that a Newmark scheme, even though it is second order accurate in time, it is not able to mitigate the non-physical modes, while a first order BDF1 scheme is too dissipative and can mask physical oscillations. It is important to remark that BDF2 can also dissipate physical oscillations, but to a much lesser extend, since it is a second order algorithm. Therefore, in this case a time step size of $\delta t = 0.002$ s has been chosen to retain the physical oscillations. The cases are run for the irreducible and the stabilized S-OSGS mixed formulation. A graphical description of the deformation and the PK2 stress field for the irreducible and S-OSGS formulations are shown in Figs. 6 and 7, respectively, using Mesh 2 for eight different time frames. The mixed formulation approach provides smoother stress fields and is able to capture stress concentration with increased precision near the clamped base of the column.

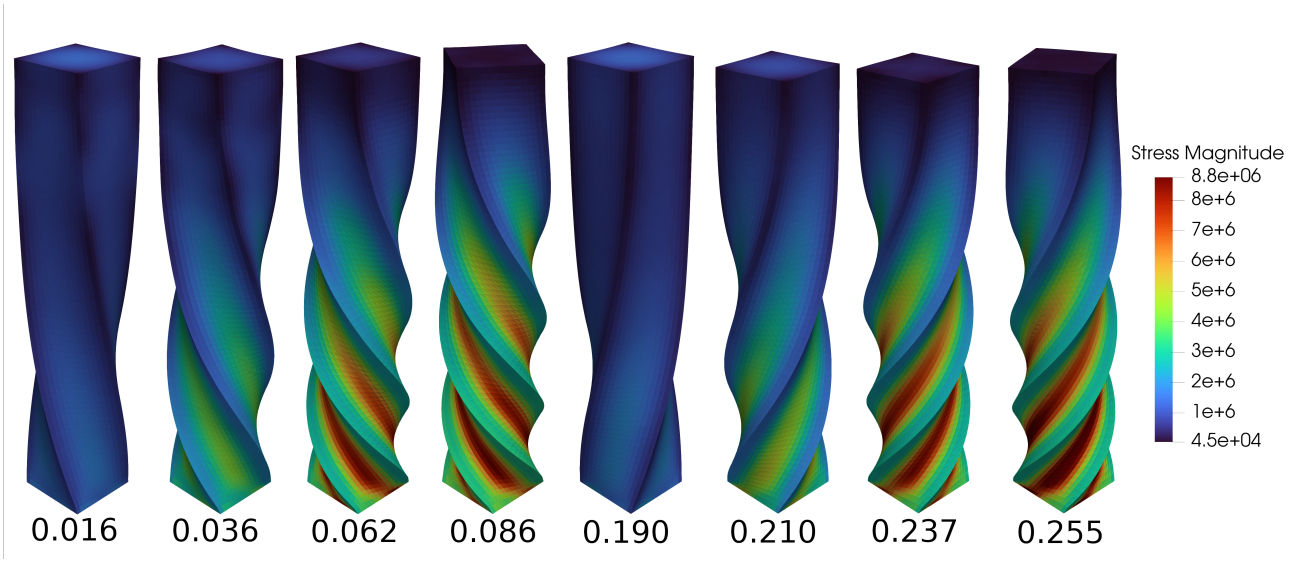

Figure 6: Twisting column: deformation and PK2 stress field in the irreducible formulation, at different times.

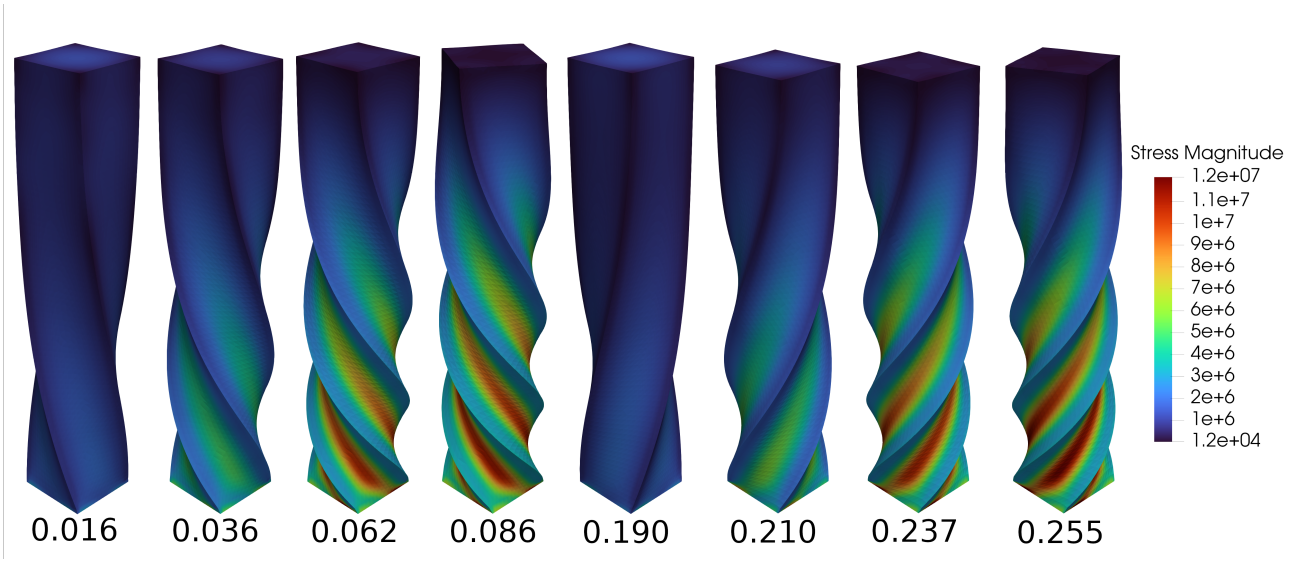

Figure 7: Twisting column: deformation and PK2 stress field in the S-OSGS mixed formulation, at different times.

The time evolution of both displacement and PK2 stress at point A, of coordinates $[0.5, 0, 3]$ m are shown in Fig. 8. Displacements converge in a similar manner upon mesh refinement using any formulation. With regards to the PK2 stresses, the irreducible formulation shows an unstable behavior at the beginning of the computation that dissipates as it advances through time, a behavior that is not present when using the S-OSGS stabilization. Stresses can be subject to concentration or singularities, so in order to assess this issue they are analyzed using Mesh 2. Stresses are plotted at points B and C of coordinates $[0.5, 0, 0]$ m and $[0.5, 0.5, 0]$ m, respectively, in Fig. 9. The behavior is much more unstable in the irreducible formulation, although it follows a similar trend as the stresses obtained with the S-OSGS formulation.

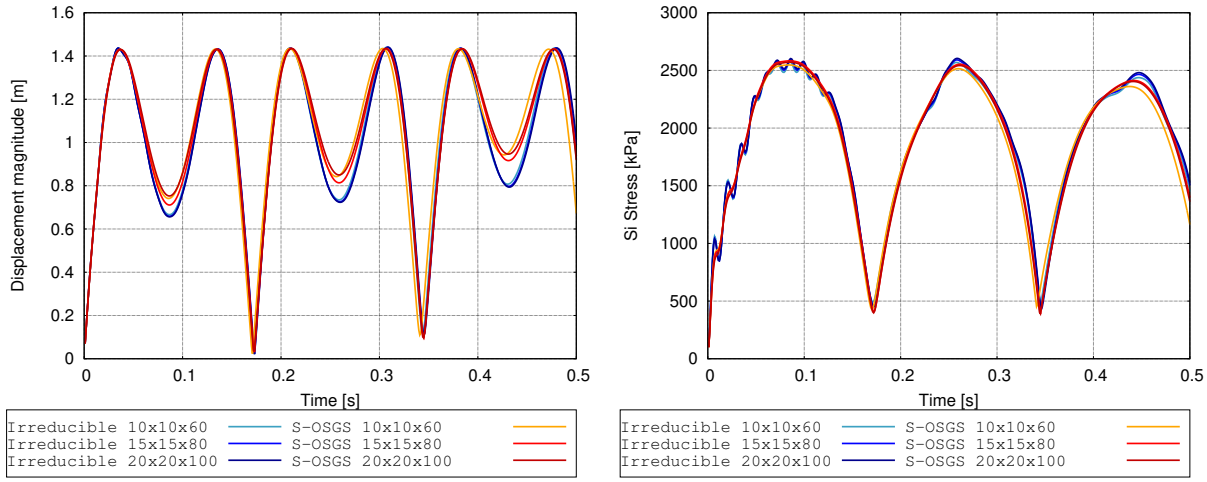

Figure 8: Twisting column: displacement (left) and PK2 stress (right) time evolution at point A.

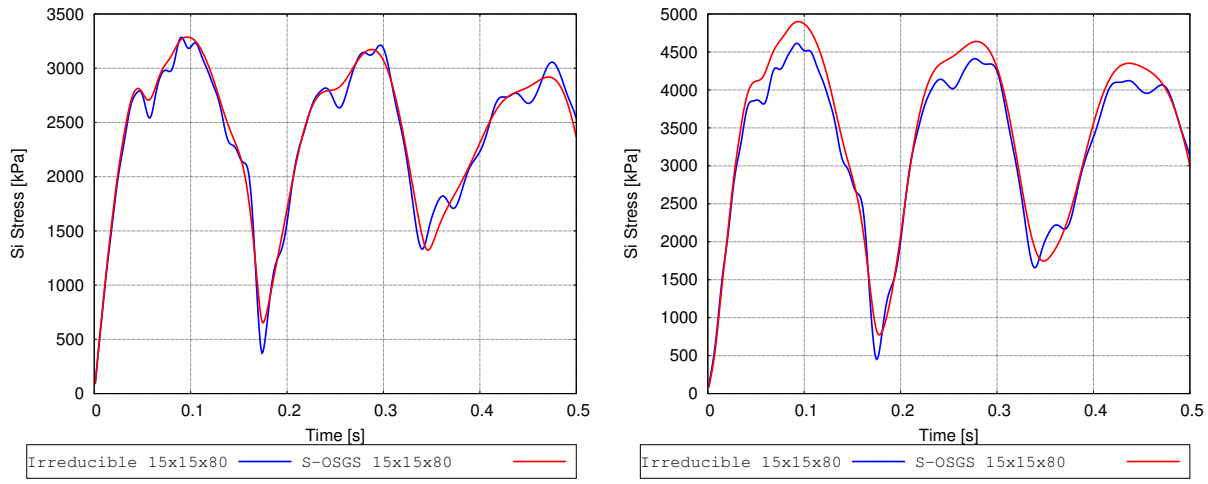

Figure 9: Twisting column: Time evolution of PK2 stress at points B (left) and C (right).

6.3. No-curvature case: Slit annular plate subject to lifting force

This is a classical benchmark to assess the performance of thin shell formulations in finite strain regimes. The problem was first proposed by Başar and Ding [38]. It consists of an annular plate slit radially, clamped in one end and subject to a lifting line force at the opposite end. The problem is set using inner and outer radius $R_i = 6\,\text{mm}$ and $R_o = 10\,\text{mm}$, respectively, and the thickness is $t = 0.03\,\text{mm}$. The material properties are $E = 2.1 \cdot 10^4\,\text{kN/mm}^2$ for the Young modulus and $\nu = 0$ for the Poisson ratio. The line force is set upwards in the transverse direction with a value of $q = 0.8\,\text{N/mm}$, and the deformation is tracked in every load increment at the point A, as portrayed in Fig.10.

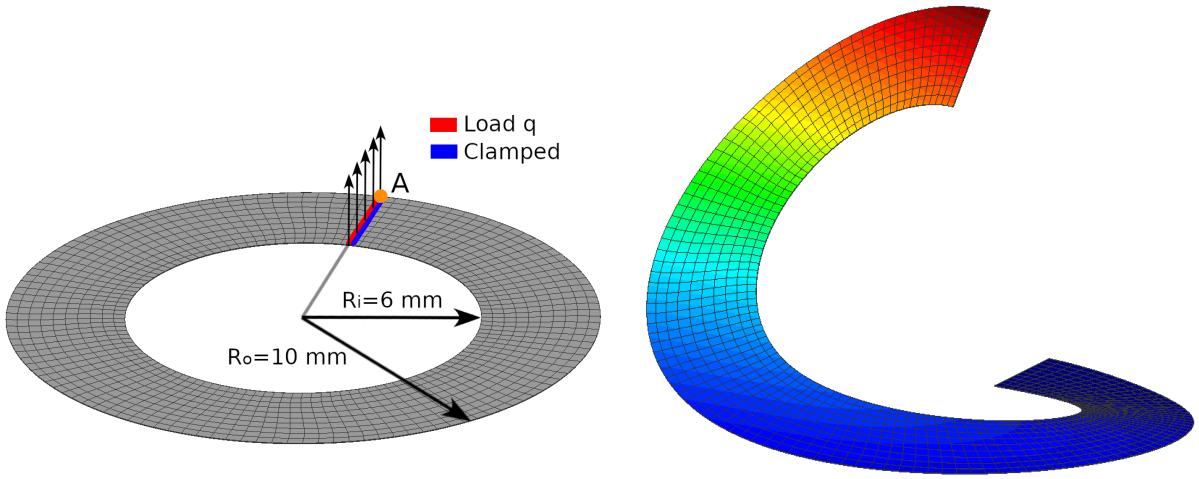

Figure 10: Slit annular plate: geometry, mesh and boundary conditions.

The problem is solved using the stabilized S-OSGS and the irreducible formulations with linear elements and quadratic hexahedral elements, respectively. The mesh is built using 10 radial elements and an increasing number of elements along the perimeter, resulting in four different meshes of 10×20, 10×40, 10×80 and 10×120 elements, with two elements in the thickness direction. Computations are performed using load factor increments of size 0.02 from 0 to 1 to track the evolution of the deformed configuration, portrayed in Fig. 11. Results are similar for both formulations, with displacements of 17.201 and 13.594 at points A and B, respectively, which show good agreement with the literature [39, 40, 41]. It is important to remark the fact that the mixed formulation converges at a similar rate compared to the irreducible formulation even though they use different orders of interpolation.

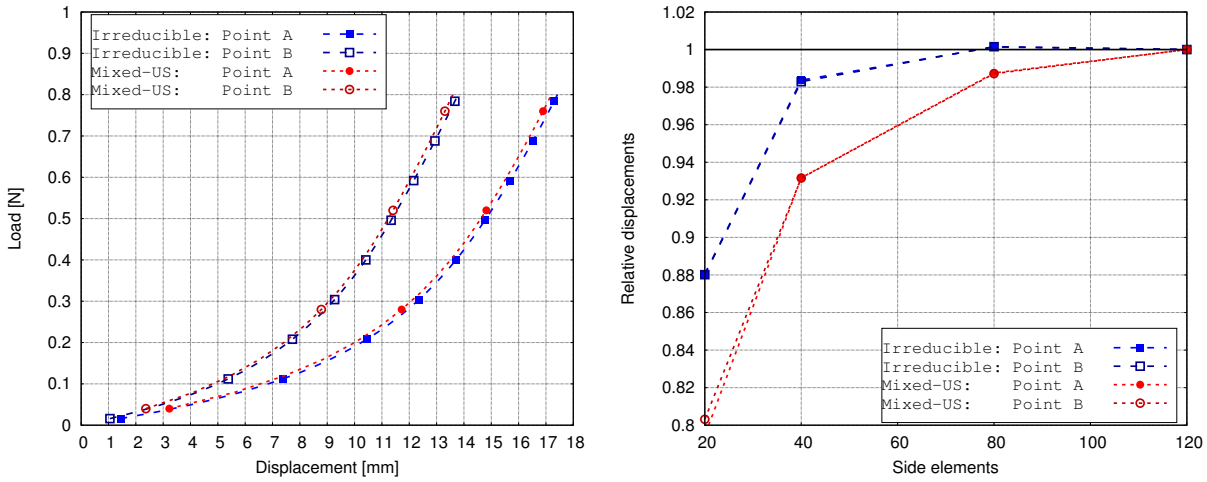

Figure 11: Slit annular plate: displacements and convergence with respect to the number of elements.

6.4. Single-curvature case: Hyperelastic cylinder

This benchmark problem was originally proposed by Büchter et al. [42] and since then became a standard case to test shell formulations in finite strain shells. The problem consists of an open-ended cylinder of length $L = 30\,\text{cm}$ and radius $R = 9\,\text{cm}$ and thickness $t = 0.2\,\text{cm}$, resting in a rigid support, and subjected to a line force q kN/m from above in a closing direction. The geometry, mesh and boundary conditions are illustrated in Fig. 12. Due to symmetry, only the eighth part of the cylinder is modeled using appropriate symmetry boundary conditions. The material is defined as Neo-Hookean with $\mu = 60\,\text{kN/mm}^2$ and $\lambda = 240\,\text{kN/mm}^2$, which correspond to a Young modulus of $E = 168\,\text{kN/mm}^2$ and a Poisson's ratio of $\nu = 0.4$.

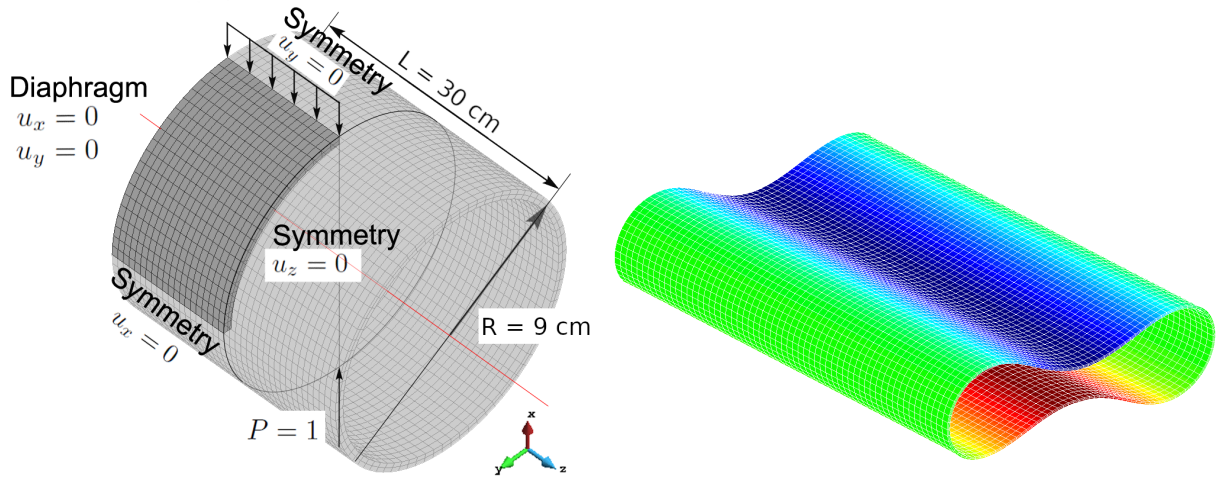

Figure 12: Hyperelastic cylinder: geometry, mesh and boundary conditions.

The problem is solved using the stabilized S-OSGS and the irreducible formulations with linear elements and quadratic hexahedral elements, respectively. The domain is discretized using meshes of 20×20, 40×40, 60×60 and 80×80 elements with two elements in the thickness direction. Results are compared using the vertical displacement tracked at point A with respect to the total load $P = qL$ as the deformation advances through small increment factors of 0.05 from 0 to 1 to have a good resolution of the evolution, as portrayed in Fig. 13.

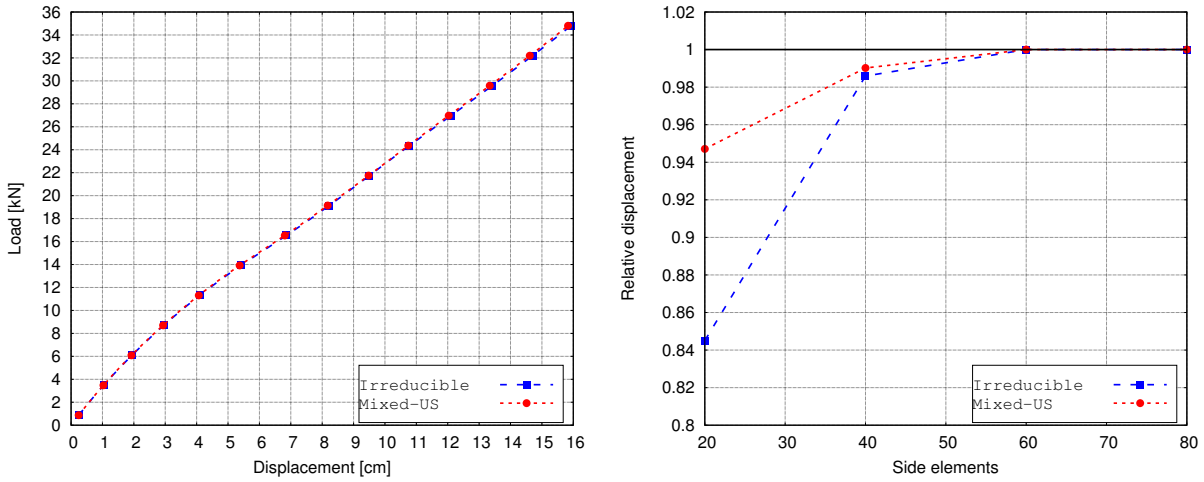

Figure 13: Hyperelastic cylinder: displacements and convergence respect to number of elements.

In the literature it is usual to measure the total load necessary to obtain a displacement of 16 cm, which is achieved with $P = 34.80\,\text{kN}$ and $P = 35.12\,\text{kN}$ in the irreducible and stabilized mixed formulation, respectively. This corresponds with the values reported in the literature [42, 43, 44, 45]. Lastly, the stabilized formulation shows a slightly faster convergence compared to the quadratic irreducible formulation.

6.5. Double-curvature case: Hemispherical shell

This benchmark problem is usually used to test inextensible membrane and bending modes in shell elements [46, 47]. It consists of a hemisphere of radius $R = 10\text{mm}$ and thickness $t = 0.04\text{mm}$ with a 18° hole with respect to the Z-axis at the top. The structure is subject to two pairs of diametrical opposite forces $P = 1\,\text{N}$ along the X and Y axes. The geometry, mesh and boundary conditions are depicted in Fig. 14. Due to the symmetry of the problem, only a quarter of the hemisphere is modelled with appropriate symmetry boundary conditions. The material is set as Neo-Hookean with $\lambda = 0.039375\,\text{kN/mm}^2$ and $\mu = 0.02625\,\text{kN/mm}^2$, which correspond to a Young modulus $E = 0.06825\,\text{kN/mm}^2$ and a Poisson's ratio $\nu = 0.3$.

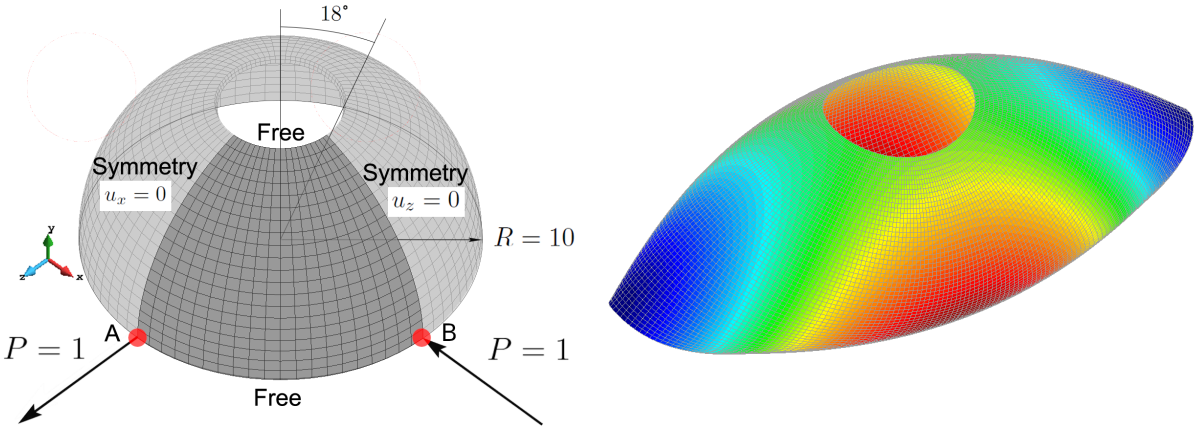

Figure 14: Hemispherical shell: geometry, mesh and boundary conditions.

The problem is solved using the stabilized S-OSGS and the irreducible formulations with linear elements and quadratic hexahedral elements, respectively. The domain is discretized using meshes of 20×20, 40×40, 60×60 and 80×80 elements with two elements along the thickness direction. The horizontal displacements are tracked at points A and B located at the points where the loads are applied, as indicated in Fig. 14. The load increases by increments of 5 from 0 to 400 to have a detailed description of the evolution. Results show good agreement with the literature [39, 48, 49, 40] as the displacements converge to 4.059 cm and 8.155 cm at points A and B, respectively.

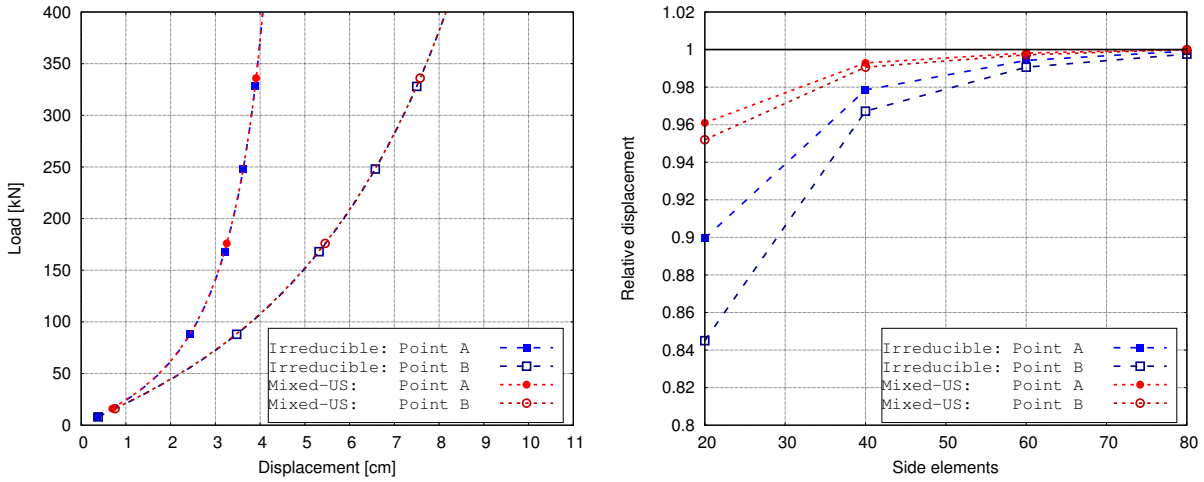

Figure 15: Hemispherical shell: displacements and convergence respect to number of elements.

7. Conclusion

A stabilized FE formulation based on the Variational Multiscale framework is proposed for dealing with solid compressible materials and thin solid-shell structures in the finite strain regime. The two-field formulation is approached using two different residual-based stabilization techniques: the Algebraic and Orthogonal Sub-Grid Scales and the term-by-term Split-Orthogonal Sub-Grid Scales. These stabilized formulations offer several advantages over the displacement-based formulation. Firstly, they overcome the space compatibility restrictions associated with the interpolation of the unknowns, providing the freedom to choose any combination of interpolating spaces. Additionally, they enable the retention of quadratic order convergence in the displacement field and increase the convergence rate from 1 to 1.5 in the PK2 stress field. This results in a significantly enhanced accuracy of the PK2 stress field, albeit with a slightly reduced accuracy of the displacement field. Furthermore, the stabilized formulations have demonstrated greater robustness, even in coarse meshes. Moreover, these formulations are quasi-static in nature but can accurately represent dynamic behavior, surpassing the capabilities of irreducible formulations. However, when much smaller time steps are required, the inclusion of dynamic SGSs may become necessary to ensure accuracy.

In the context of shells, it is well-known that thin structures approximated using solid-shell elements are prone to various types of numerical locking. However, even in the case of extremely thin structures in the finite strain regime, the stabilized formulation effectively addresses numerical locking issues and enables a more accurate representation of the deformation state compared to a quadratic element irreducible formulation. The significant advantage of utilizing the stabilized two-field formulation in solid-shell elements for shell problems is that it preserves all the enhancements provided for solid elements, while eliminating the need for additional constraints typically present in classical shell formulations.

Acknowledgements

This work was supported by Vicerrectoría de Investigación, Desarrollo e Innovación (VRIDEI) of the Univeridad de Santiago de Chile, and the National Agency for Research and Development (ANID) Doctorado Becas Chile/2019 - 72200128 of the Government of Chile. I. Castañar gratefully acknowledges the support received from the Agència de Gestió d'Ajut i de Recerca through the predoctoral FI grant 2019-FI-B-00649. R. Codina gratefully acknowledges the support received through the ICREA Acadèmia Research Program of the Catalan Government. This work was partially funded through the TOPFSI-APP: Ref. PDC2022-133581-I00 MICINN of the Spanish Government. CIMNE is a recipient of a "Severo Ochoa Programme for Centers of Excellence in R&D" grant (CEX2018-000797-S) by the Spanish Ministry of Economy and Competitiveness.

Declarations

Conflict of interest

The authors declare that they have no known competing financial interests or personal relationships that could have appeared to influence the work reported in this paper.

Replication of results

All the information required for replicating the paper results was duly presented. Data files for the results are available upon request from the authors.

References

[1] T. Belytschko, W. K. Liu, B. Moran, and K. Elkhodary, *Nonlinear finite elements for continua and structures*. John wiley & sons, 2014.

[2] M. Bischoff, K.-U. Bletzinger, W. Wall, and E. Ramm, "Models and finite elements for thin-walled structures," *Encyclopedia of computational mechanics*, 2004.

[3] A. Aguirre, R. Codina, and J. Baiges, "Stress-displacement stabilized finite element analysis of thin structures using solid-shell elements—Part I: On the need of interpolating the stresses," Submitted.

[4] E. Oñate, *Structural analysis with the finite element method. Linear statics: volume 2: beams, plates and shells*. Springer Science & Business Media, 2013.

[5] K. Sze, "Three-dimensional continuum finite element models for plate/shell analysis," *Progress in Structural Engineering and Materials*, vol. 4, no. 4, pp. 400–407, 2002.

[6] R. H. MacNeal, "Toward a defect-free four-noded membrane element," *Finite elements in analysis and design*, vol. 5, no. 1, pp. 31–37, 1989.

[7] S. Doll, K. Schweizerhof, R. Hauptmann, and C. Freischläger, "On volumetric locking of low-order solid and solid-shell elements for finite elastoviscoplastic deformations and selective reduced integration," *Engineering Computations*, vol. 17, no. 7, pp. 874–902, 2000.

[8] O. Zienkiewicz, R. Taylor, and J. Too, "Reduced integration technique in general analysis of plates and shells," *International Journal for Numerical Methods in Engineering*, vol. 3, no. 2, pp. 275–290, 1971.

[9] T. Belytschko, J. S.-J. Ong, W. K. Liu, and J. M. Kennedy, "Hourglass control in linear and nonlinear problems," *Computer Methods in Applied Mechanics and Engineering*, vol. 43, no. 3, pp. 251–276, 1984.

[10] R. H. MacNeal, "A simple quadrilateral shell element," *Computers & Structures*, vol. 8, no. 2, pp. 175–183, 1978.

[11] K. Park and G. Stanley, "A curved C^0 shell element based on assumed natural-coordinate strains," *Journal of Applied Mechanics*, vol. 53, no. 2, pp. 278–290, 1986.

[12] J. C. Simo and M. Rifai, "A class of mixed assumed strain methods and the method of incompatible modes," *International journal for numerical methods in engineering*, vol. 29, no. 8, pp. 1595–1638, 1990.

[13] T. Belytschko and L. P. Bindeman, "Assumed strain stabilization of the eight node hexahedral element," *Computer Methods in Applied Mechanics and Engineering*, vol. 105, no. 2, pp. 225–260, 1993.

[14] E. N. Dvorkin and K.-J. Bathe, "A continuum mechanics based four-node shell element for general non-linear analysis," *Engineering computations*, vol. 1, no. 1, pp. 77–88, 1984.

[15] D. Chapelle, A. Ferent, and K. Bathe, "3d-shell elements and their underlying mathematical model," *Mathematical Models and Methods in Applied Sciences*, vol. 14, no. 01, pp. 105–142, 2004.

[16] D. Boffi, F. Brezzi, M. Fortin, *et al.*, *Mixed finite element methods and applications*, vol. 44. Springer, 2013.

[17] T. J. Hughes, "Multiscale phenomena: Green's functions, the Dirichlet-to-Neumann formulation, subgrid scale models, bubbles and the origins of stabilized methods," *Computer methods in applied mechanics and engineering*, vol. 127, no. 1-4, pp. 387–401, 1995.

[18] T. J. Hughes, G. R. Feijóo, L. Mazzei, and J.-B. Quincy, "The variational multiscale method—A paradigm for computational mechanics," *Computer methods in applied mechanics and engineering*, vol. 166, no. 1-2, pp. 3–24, 1998.

[19] R. Codina, "Stabilization of incompressibility and convection through orthogonal sub-scales in finite element methods," *Computer methods in applied mechanics and engineering*, vol. 190, no. 13-14, pp. 1579–1599, 2000.

[20] E. Castillo and R. Codina, "Finite element approximation of the viscoelastic flow problem: A non-residual based stabilized formulation," *Computers & Fluids*, vol. 142, pp. 72–78, 2017.

[21] L. Moreno, R. Codina, J. Baiges, and E. Castillo, "Logarithmic conformation reformulation in viscoelastic flow problems approximated by a VMS-type stabilized finite element formulation," *Computer Methods in Applied Mechanics and Engineering*, vol. 354, pp. 706–731, 2019.

[22] E. Castillo and R. Codina, "Dynamic term-by-term stabilized finite element formulation using orthogonal subgrid-scales for the incompressible Navier-Stokes problem," *Computer Methods in Applied Mechanics and Engineering*, vol. 349, pp. 701–721, 2019.

[23] I. Castañar, J. Baiges, and R. Codina, "A stabilized mixed finite element approximation for incompressible finite strain solid dynamics using a total Lagrangian formulation," *Computer Methods in Applied Mechanics and Engineering*, vol. 368, p. 113164, 2020.

[24] I. Castañar, R. Codina, and J. Baiges, "A stabilized mixed three-field formulation for stress accurate analysis including the incompressible limit in finite strain solid dynamics," *International Journal for Numerical Methods in Engineering*, vol. 124, no. 10, pp. 2341–2366, 2023.

[25] I. Castañar, J. Baiges, R. Codina, and H. Venghaus, "Topological derivative-based topology optimization of incompressible structures using mixed formulations," *Computer Methods in Applied Mechanics and Engineering*, vol. 390, p. 114438, 2022.

[26] A. Fabra and R. Codina, "Mixed stabilized finite element methods in linear elasticity for the velocity–stress equations in the time and the frequency domains," *Computer Methods in Applied Mechanics and Engineering*, vol. 404, p. 115777, 2023.

[27] A. Aguirre, R. Codina, and J. Baiges, "A variational multiscale stabilized finite element formulation for Reissner–Mindlin plates and Timoshenko beams," *Finite Elements in Analysis and Design*, vol. 217, p. 103908, 2023.

[28] S. Saloustros, M. Cervera, S. Kim, and M. Chiumenti, "Accurate and locking-free analysis of beams, plates and shells using solid elements," *Computational Mechanics*, vol. 67, no. 3, pp. 883–914, 2021.

[29] R. Codina, J. Principe, and J. Baiges, "Subscales on the element boundaries in the variational two-scale finite element method," *Computer Methods in Applied Mechanics and Engineering*, vol. 198, no. 5-8, pp. 838–852, 2009.

[30] R. Codina, "Finite element approximation of the three-field formulation of the Stokes problem using arbitrary interpolations," *SIAM Journal on Numerical Analysis*, vol. 47, no. 1, pp. 699–718, 2009.

[31] C. Bayona, J. Baiges, and R. Codina, "Variational multi-scale finite element approximation of the compressible Navier-Stokes equations," *International Journal of Numerical Methods for Heat & Fluid Flow*, vol. 26, no. 3/4, pp. 1240–1271, 2016.

[32] M. Cervera, M. Chiumenti, and R. Codina, "Mixed stabilized finite element methods in nonlinear solid mechanics: Part I: Formulation," *Computer Methods in Applied Mechanics and Engineering*, vol. 199, no. 37-40, pp. 2559–2570, 2010.

[33] M. Chiumenti, M. Cervera, and R. Codina, "A mixed three-field fe formulation for stress accurate analysis including the incompressible limit," *Computer Methods in Applied Mechanics and Engineering*, vol. 283, pp. 1095–1116, 2015.

[34] R. Codina, "On stabilized finite element methods for linear systems of convection–diffusion-reaction equations," *Computer Methods in Applied Mechanics and Engineering*, vol. 188, no. 1-3, pp. 61–82, 2000.

[35] R. Codina, "Stabilized finite element approximation of transient incompressible flows using orthogonal subscales," *Computer methods in applied mechanics and engineering*, vol. 191, no. 39-40, pp. 4295–4321, 2002.

[36] J. Bonet, A. J. Gil, C. H. Lee, M. Aguirre, and R. Ortigosa, "A first order hyperbolic framework for large strain computational solid dynamics. Part I: Total lagrangian isothermal elasticity," *Computer Methods in Applied Mechanics and Engineering*, vol. 283, pp. 689–732, 2015.

[37] A. J. Gil, C. H. Lee, J. Bonet, and R. Ortigosa, "A first order hyperbolic framework for large strain computational solid dynamics. Part II: Total lagrangian compressible, nearly incompressible and truly incompressible elasticity," *Computer Methods in Applied Mechanics and Engineering*, vol. 300, pp. 146–181, 2016.

[38] Y. Başar and Y. Ding, "Finite-rotation elements for the non-linear analysis of thin shell structures," *International Journal of Solids and Structures*, vol. 26, no. 1, pp. 83–97, 1990.

[39] K. Sze, W. Chan, and T. Pian, "An eight-node hybrid-stress solid-shell element for geometric non-linear analysis of elastic shells," *International Journal for Numerical Methods in Engineering*, vol. 55, no. 7, pp. 853–878, 2002.

[40] M. Mostafa, M. Sivaselvan, and C. Felippa, "A solid-shell corotational element based on ANDES, ANS and EAS for geometrically nonlinear structural analysis," *International journal for numerical methods in engineering*, vol. 95, no. 2, pp. 145–180, 2013.

[41] Z. Li, J. Huang, S. Cen, and C.-F. Li, "An unsymmetric 8-node hexahedral solid-shell element with high distortion tolerance: Geometric nonlinear formulations," *International Journal for Numerical Methods in Engineering*, vol. 120, no. 5, pp. 580–606, 2019.

[42] N. Büchter, E. Ramm, and D. Roehl, "Three-dimensional extension of non-linear shell formulation based on the enhanced assumed strain concept," *International journal for numerical methods in engineering*, vol. 37, no. 15, pp. 2551–2568, 1994.

[43] K. Sze, S.-J. Zheng, and S. Lo, "A stabilized eighteen-node solid element for hyperelastic analysis of shells," *Finite Elements in Analysis and Design*, vol. 40, no. 3, pp. 319–340, 2004.

[44] M. Schwarze and S. Reese, "A reduced integration solid-shell finite element based on the EAS and the ANS concept. Large deformation problems," *International Journal for Numerical Methods in Engineering*, vol. 85, no. 3, pp. 289–329, 2011.

[45] J. Kiendl, M.-C. Hsu, M. C. Wu, and A. Reali, "Isogeometric Kirchhoff–Love shell formulations for general hyperelastic materials," *Computer Methods in Applied Mechanics and Engineering*, vol. 291, pp. 280–303, 2015.

[46] N. Stander, A. Matzenmiller, and E. Ramm, "An assessment of assumed strain methods in finite rotation shell analysis," *Engineering Computations*, vol. 6, no. 1, pp. 58–66, 1989.

[47] H. C. Park, C. Cho, and S. W. Lee, "An efficient assumed strain element model with six dof per node for geometrically non-linear shells," *International Journal for Numerical Methods in Engineering*, vol. 38, no. 24, pp. 4101–4122, 1995.

[48] S. Klinkel, F. Gruttmann, and W. Wagner, "A robust non-linear solid shell element based on a mixed variational formulation," *Computer methods in applied mechanics and engineering*, vol. 195, no. 1-3, pp. 179–201, 2006.

[49] M. Schwarze and S. Reese, "A reduced integration solid-shell finite element based on the EAS and the ANS concept. Geometrically linear problems," *International Journal for Numerical Methods in Engineering*, vol. 80, no. 10, pp. 1322–1355, 2009.